Shallow portion of an active geothermal system revealed by multidisciplinary studies: the case of Le Biancane (Larderello, Italy)

Domenico Granieri[a,*], Francesco Mazzarini[a], Matteo Cerminara[a], Benedetta Calusi[a], Andrea Scozzari[c], Matia Menichini[b], Matteo Lelli[a,b]

[a] Istituto Nazionale di Geofisica e Vulcanologia, Sezione Pisa, via C. Battisti, 53, 56125 Pisa, Italy

[b] CNR-IGG Istituto di Geoscienze e Georisorse, Via G. Moruzzi 1, 56124 Pisa, Italy

[c] CNR-ISTI Istituto di Scienza e Tecnologie dell'Informazione, Via G. Moruzzi 1, 56124 Pisa, Italy

* Corresponding author - D. Granieri
E-mail address: domenico.granieri@ingv.it
Postal address: Istituto Nazionale di Geofisica e Vulcanologia, Sezione Pisa, via C. Battisti, 53, 56125 Pisa, Italy

Abstract

The natural park of Le Biancane is located in the southern sector of the Larderello-Travale geothermal field (LTGF). It extends over an approximately 100,000 m^2 area where the impermeable caprock is locally absent and deep fluids may directly reach the surface. Through a multidisciplinary approach including measurements of soil CO_2 flux (total output of 11.5 t day^{-1}), soil temperature (average 34.4 °C), stable isotope and chemical data on fluids from fumaroles (dominated by a mixture of geothermal gases and air or gases from air-saturated meteoric water), and structural analysis of the formation outcropping, we found that anomalous CO_2 emissions are positively correlated with shallow temperature anomalies. These are in restricted locations adjacent to vents and fumaroles, where a network of well-connected fractures (preferentially NW-SE and NE-SW orientated and with steep dips) drains efficiently allowing upward migration of the deep fluids and the energy toward the surface.

1. Introduction

Geothermal fields are characterized by hot and pressurized fluids basically composed by dry steam or, more frequently, by hot water and vapour, usually followed in mass abundance by CO_2, H_2S, CH_4, NH_3, and Hg (Giggenbach, 1992). Typically, the fluids remain confined within the reservoir(s) because of an impervious covering and they can be extracted by wells in exploitation of the geothermal field. However, the system is never fully sealed either because faults and fractures of the covering may provide pathways for the upward migration of deep gases and/or because the impermeable caprock is locally missing through erosive or tectonic processes. In these cases, the fluid may naturally reach the surface and generate diffuse degassing from the soil, notably of CO_2 that represents the main constituent of non-condensable gases. Alternatively, the steam rising with non-condensable gases condenses at the base of the caprock enhancing the heat transfer by conduction within a thin near-surface soil layer where a steep temperature gradient develops (Hochstein and Bromley, 2005; Hochstein and Browne, 2000). Locally, where the caprock is fractured, the steam discharges the heat advectively through cracks, vents and fumaroles (Hochstein and Bromley, 2005; Hurwitz et al., 2012). In both cases, the heat transfer raises the temperature of the ground surface that can be mapped by infra-red (IR) techniques, with highest chances of success in presence of “bare ground”, namely hot ground not covered by vegetation (Hochstein and Bromley, 2005).

Migration of fluids in the crust is a prerequisite for many geologic processes such as regional metamorphism and formation of hydrothermal, geothermal, plutonic, and volcanic systems, as well as ore deposits (Baba et al., 2019; Cox, 2010; Hardebol et al., 2015; McNamara et al., 2019; Moeck, 2014; Oliver, 1996). In geothermal systems, secondary permeability due to a fracture network frequently controls the fluid flow (see Bertini et al., 2006; Cerminara and Fasano, 2012; Cox, 2010; Gianelli et al., 1997; Gudmundsson et al., 2002; Siler et al., 2016;

Uzelli et al., 2017, 2021). A fracture network can be regarded as a system of fractures developed within the rock volume and may involve a number of distinct fracture sets which may or may not intersect. Fractures hierarchies and abutment relationships as well as spatial orientation and length distribution control the fracture connectivity that, in turn, strongly controls the permeability of the reservoir (Adler and Thovert, 1999; Barton, 1995; Hardebol et al, 2015; Sanderson and Nixon, 2015). A network of fractures generally varies in the spatial distribution over time (e.g. Adler and Thovert, 1999).

Resident time of fluids in geothermal reservoir(s) is generally long enough to attain chemical equilibrium at depth (Chiodini and Marini, 1998). During upflow from the geothermal reservoir(s) to the surface physico-chemical secondary processes due to different thermodynamic conditions encountered along the flow-path may trigger chemical and isotope modifications of the geothermal fluids. In high vertical permeability conditions, the rapid ascent of geothermal fluids along fractures and faults can prevent significant changes of chemical and isotope compositions (Baba et al., 2022; Chiodini and Marini, 1998), confirming in that case the pivotal role of the connected fracture networks in the fluid circulation.

The Larderello-Travale Geothermal Field (LTGF) was the first in Italy (Tuscany) and in the entire world used for the production of electricity (starting from 1913) and remains the most important vapour-dominated geothermal field in Europe and among the first in the world (Bertani, 2016). According to Moeck (2014) LTGF is a convection-dominated plutonic geothermal type play. In this type of play a pluton derived from the magma crystallization and slowly cooling below the surface is the main source of heat and geothermal fluids whose migration to the surface is mainly controlled by structural factors (Moeck, 2014). Recently, monodisciplinary investigations have been made in the LTGF to estimate the soil CO_2 degassing (e.g., Cabassi et al., 2021; Venturi et al., 2019), to monitor the surface temperatures

through satellite and in-situ thermal images (Silvestri et al., 2020), and to define the nature of the local seismicity by analysing a large dataset of microearthquakes (Piccinini and Saccorotti, 2018). The recent study of Taussi et al. (2022) integrated geochemical and geological information to highlight relations among fractures, soil degassing and heat output in a limited sector of the LTGF.

In this study, we propose a multidisciplinary approach involving geochemical and structural investigations in order to determine the relations between surface gas emission, T and P equilibrium conditions at the deep source of gases, warming of the soil, and structural features of the shallow portion of the LTGF. Geochemical data, in particular soil CO_2 flux also used as tracer of the vapour output and thus of the heat flow, and other information on surficial structures and thermal conditions of the soils were examined in an effort to provide the necessary constraints to the physical modelling of the local fluid circulation and heat release. Moreover, we produced new data regarding the geochemical composition of the local natural manifestations, revealing for the first time in such manifestations the carbonyl sulphide (COS) content that is a useful parameter to better constrain the P conditions at depth. As a test site, we selected Le Biancane natural park, 12 km south of the Larderello village and fully included in the LTGF. This area is characterized by bare and locally steaming soils, high temperature fumaroles, hot springs and some hot and acidic mud pools (here named "lagoni").

2. Le Biancane study area in the geological, structural and geothermal setting of the Larderello Travale Geothermal Field (LTGF)

The LTGF is located in the inner part of the Northern Apennines (Italy). The geological setting of the geothermal field consists (Fig. 1a,b) of a stack of Alpine tectonic units (Ligurian Units and Tuscan Nappe), which overlie the Tuscan Metamorphic Basement, a

107 buried complex of low-grade metamorphic units made up of terrigenous and carbonatic
108 successions of Permian-Triassic (Musumeci et al., 2002) and Palaeozoic rocks (Batini et al.,
109 1983). Since the Pliocene, the emplacement of granites in the metamorphic tectonic units led
110 to the development of broad low pressure - high temperature (0.15-0.2 GPa – 500-650 °C)
111 contact aureoles with development of medium to high grade hornfels rocks and associated
112 hydrothermal systems (Carella et al., 2000; Cavaretta et al., 1983; Gianelli et al., 1997;
113 Gianelli and Ruggeri, 2002; Musumeci et al., 2002). The geothermal system, located at
114 depths between 500 m and 4000 m, evolved from an early stage, coeval with granitic
115 intrusions, dominated by magmatic and metamorphic fluids, to the present-day stage
116 dominated by meteoric fluids (Ruggieri et al., 1999). A noteworthy feature of the geothermal
117 field is the K-Horizon (Fig. 1b), a regional-scale seismic reflector recognized at the 3-8 km
118 depth range, at the top of Quaternary granites (Batini et al., 1978, 1985; Bertini et al., 2006).
119 This reflector is characterized by a strong amplitude bright-spot signal, suggesting the
120 presence of fluids of magmatic and/or metamorphic origin hosted within cracks and/or micro-
121 cracks (Batini et al., 1983; Gianelli et al., 1997). At shallower depths (2-4 km), there is
122 another reflective marker, the so-called H-horizon, corresponding to the contact aureola of
123 the Pliocene granites (Bertini et al., 2006).
124 The explored area of the Larderello geothermal field is about 250 km^2, and produces about
125 4300 t h^{-1} (tons per hour) of superheated steam at temperatures between 150-270 °C and
126 pressures of 0.2-1.8 MPa, associated to an average content of non-condensable gas ranging
127 from 1 to 15% by weight (Razzano and Cei, 2015). The adjacent explored area of Travale
128 covers approximately 50 km^2 and produces a total of 1300 t h^{-1} of superheated steam at 190-
129 250 °C and 0.8-2 MPa pressure, with a content of non-condensable gas in the range 4-8% by
130 weight (Razzano and Cei, 2015). Both fields are connected to a unique deeper geothermal
131 reservoir, located in the Paleozoic metamorphic units (Bertini et al., 2006), representing the

exploited reservoir at the present (Fig. 1b). This unique geothermal system can be delimited by the 300 °C isotherm, which at 3000 m depth includes an area of over 400 km^2 extending from the western margin of the Larderello field to the Travale area (Bertini et al., 2005). In the past (up to about 30 years ago) the geothermal resource of the Larderello-Travale area was extracted from the upper reservoir, hosted within Mesozoic limestones of the Tuscan Nappe at depths of 500-1500 m and capped by an impervious covering of the clayey Ligurian Units (Liotta and Brogi, 2020). Faults in the LTGF are mainly normal faults associated with the latest extensional episode which is lasting since the late Pliocene (Brogi et al., 2003). Faulting affects different crustal levels with major NW-SE trending normal faults and NE-SW trending oblique to strike-slip steeply dipping faults (Liotta and Brogi, 2020).

In the southern part of the LTGF, where Le Biancane area lies, the carbonate-anhydrite formations of the Tuscan Nappe outcrops (Fig. 1b,c), allowing the infiltration of meteoric water to depth, thus partially feeding the shallow reservoir (Ceccarelli et al., 1987). The possible interference zones between meteoric water infiltration and deeper geothermal fluids have been indicated by the presence of liquid water instead of vapour in exploration wells and at times by thermal inversion at the field boundaries (Arias et al., 2010). The same authors estimated, by means of the gas/steam ratio, that the total steam flow rate from local recharge is about 390-580 t h^{-1} (i.e., 3.3 - 5.0*10^6 m^3 y^{-1}) for the whole LTGF system.

A Land Surface Temperature (LST) map retrieved by satellite data shows that a thermal anomaly is centred at Le Biancane and it extends northwards in the adjacent thermal area of Sasso Pisano village (Fig. 1d).

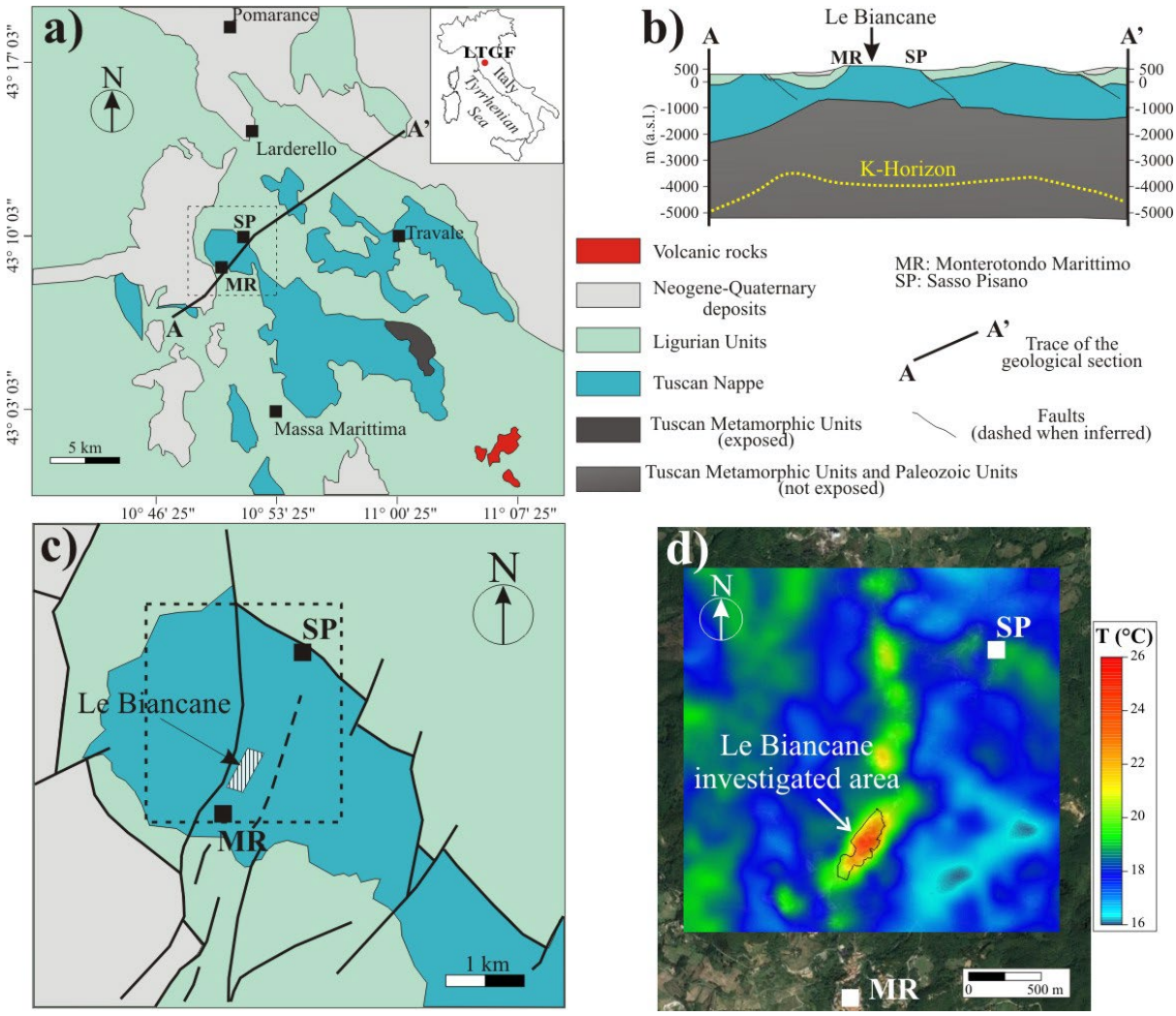

Figure 1. a) Geologic sketch map of the Larderello-Travale Geothermal Field (modified after Liotta and Brogi, 2020). The red dot in the inset is the location of the LTGF; the dotted black box is zoomed in Fig. 1c. b) Geological sketch section (A-A' in Fig. 1a; modified after Arias et al., 2010 and Liotta and Brogi, 2020). c) Geological and tectonic sketch map of Le Biancane area (modified after Liotta and Brogi, 2020); the dotted black box is zoomed in Fig. 1d). d) Map of Land Surface Temperature derived from the scene acquired on 15 June 2021 at 20:59 UTC by the TIRS (Thermal InfraRed Sensor) instrument, onboard the Landsat8 mission, applying the atmospheric corrections described in Barsi et al. (2003). A constant emissivity (ϵ_r=0.97) has been hypothesized for the whole scene, to improve the temperature estimation in the pixels where the land coverage class is mostly bare soil.

3. Field activities at Le Biancane and methodologies

Field activities at Le Biancane were performed to characterize the process of CO_2 degassing and heating from local soils, also identifying fault-related anisotropies in their spatial

distributions.

The surveys were conducted during the local dry season, in May-June, 2021 and included: i) 197 soil CO_2 flux measurements over a grid of ~ 60,000 m^2 covering the main degassing area of Le Biancane and immediate surroundings; ii) 146 soil brightness temperature measurements through thermal IR imaging over the degassing area; iii) sampling and analysis of three fumaroles falling in Le Biancane area; iv) structural analysis of the local fracture systems and their relationships with the bedding planes at 46 points (Fig. 2 a,b).

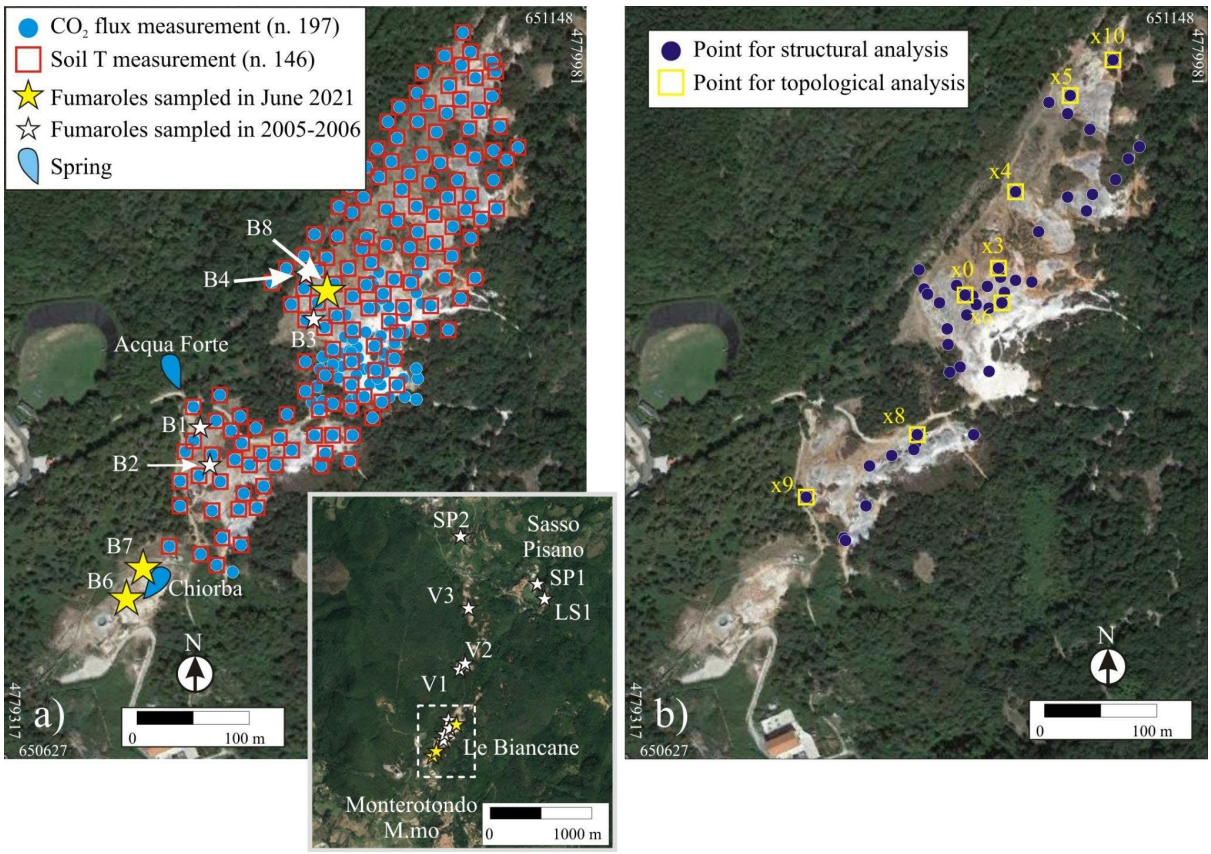

Figure 2. Aerial pictures (from Google Earth®) of Le Biancane study area showing the locations of a) Soil CO_2 flux, soil temperature, fumaroles and springs sites. b) Points for structural and topological analysis. Inset of a) shows the locations of the fumaroles at Le Biancane (dashed rectangle) and in the Sasso Pisano area. The images are hereafter projected in the Universal Transverse Mercator (UTM) geographic coordinates, datum WGS 1984, zone 32°N.

3.1. Soil CO_2 flux and soil temperature measurements and data treatment

184 Soil CO_2 flux and soil brightness temperature measurements were taken at Le Biancane to
185 quantify the CO_2 output from the soil and to investigate potential relationships between the
186 spatial pattern produced by high CO_2 flux and elevated shallow soil temperatures.
187 The soil CO_2 flux measurements were made through the accumulation chamber method
188 (Chiodini et al., 1998) and punctual measurements were treated with the sequential Gaussian
189 simulation (sGs) approach (Cardellini et al., 2003) to provide the spatial distribution of the
190 soil CO_2 degassing and the quantitative estimate of the total CO_2 output. In addition, the CO_2
191 flux measurements were arranged on logarithmic probability plots, where the unusual
192 abscissa represents units of standard deviation corresponding to different theoretical quantile
193 thresholds. As discussed by Sinclair (1974), in such plots a single lognormal population
194 would plot as a straight line, while *n* overlapping lognormal populations would result on a
195 curve with *n-1* inflection points. The procedure of Sinclair (1974) permits to recognize the
196 presence of mixtures of more populations and to separate each of them through the estimation
197 of the relative proportion, the median and the standard deviation. Since the derived values
198 refer to the logarithm of the values, the median soil CO_2 flux and the 90% confidence interval
199 of the median for each population were computed by using the Sichel's t estimator (David,
200 1977).
201 In most of the sites corresponding with the CO_2 flux locations (Fig. 2a), we acquired thermal
202 images with a portable thermal IR camera (mod. FLIR E76), to infer actual ground surface
203 temperatures and to define the extent of the "anomalous" thermal area to be compared with
204 the main CO_2 degassing area (see Fig. B.1 in Appendix B for a thermal infrared view of the
205 main anomalous area). The FLIR E76 thermal camera was equipped with a 42° field of view
206 optic. Emissivity and atmospheric temperature were set at 0.98 and 20 °C, respectively, while
207 atmospheric absorption was switched off given the source proximity. The first centimetres of
208 terrain were removed before making thermal images to minimise the effects of the vegetation

209 and direct solar irradiation. The camera was operated horizontally about 1 m above the
210 ground to capture a rectangular area of 40x30 cm^2, including 160x120 pixels (Fig. B.2 in
211 Appendix B). The soil brightness temperature was then taken by averaging the temperature of
212 the pixels of the scene. Maps of brightness temperature were produced by using the same
213 statistical interpolation method used for the gas flux (i.e., the sGs approach) and the
214 representation on a probability plot was used to partition the mixture of real data into separate
215 populations by using the Sinclair (1974) procedure.
216 The emissivity of the Biancane soil was estimated to vary in the range ϵ = 0.94 - 0.99 from
217 information about soil composition and structure (Mineo and Pappalardo, 2021). This
218 uncertainty is one of the factors defining the confidence interval of the brightness
219 temperatures presented here. The brightness temperature confidence interval related to the
220 emissivity was evaluated by applying the algorithm presented in Calusi et al. 2020. When ϵ
221 ranges in the values fixed above, the difference between the soil brightness temperature and
222 the ambient temperature varies of about 2% with respect to the value obtained with an
223 average value $\epsilon = 0.965$. Thus, the absolute error due to the uncertainty in emissivity ranges
224 from negligible values when the observed temperature is similar to the ambient temperature
225 up to 2 °C for the hottest points observed at Le Biancane. This uncertainty is within the
226 instrumental error of the thermal camera used in this work.
227 The use of statistical methods appropriate for lognormally (soil CO_2 flux) or normally (soil
228 brightness temperature) distributed data has allowed for the identification of different
229 statistical populations that can be eventually related to different sources of gas and heat
230 (basically, shallow or deep sources).
231

232 **3.2. Gas sampling and analytical procedures**

233 Samples of gas were collected from three high-temperature fumaroles located within or

adjacent to the area investigated for the soil CO_2 degassing (B6, B7, and B8, Fig. 2a). Gas samples were collected in June 2021 using two different methods. The first method, was to use pre-evacuated two stop-cocks glass bottles partially filled with aqueous solution of 4.5 N sodium hydroxide (Giggenbach, 1975). The second method was to employ a glass condenser with ethyl-ether for separation of steam from non-condensable gases (Cioni et al., 1988). At each sampling point, the temperature of gas emission was measured before and after sample collection.

Chemical and isotope analyses were performed in the Institute of Geosciences and Earth Resources of the National Research Council of Italy (IGG-CNR). H_2, He, Ar, O_2, N_2 and CH_4 concentrate in the headspace of glass bottles partially filled with caustic solution and were detected using a Perkin Elmer Clarus 580 gas chromatograph equipped with capillary column, TCD and FID detectors (the last detector used for detection of low CH_4 concentrations). CO_2 and H_2S were absorbed in the sodium hydroxide aqueous solution and were determined by acid-base titration and ion chromatography, respectively, after the oxidation with hydrogen peroxide. In dry gas samples collected following the method by Cioni et al. (1988), low H_2 and CO concentrations were detected using a high-sensitivity Reduction Gas Detector (HgO; detection limit better than 0.05 ppmv), whereas COS was analysed using the high-selectivity and high-sensitivity (detection limit 0.5 ppbv) GC-ICP-MS system, coupling with special transfer line the GC Agilent 7890B with the ICP-MS Agilent 7800, as described in Lelli (2021). Dry gas samples were also used to measure the $\delta^{13}C_{CO2}$ (‰ VPDB - Vienna Pee Dee Belemnite) by means of GC-combustion interface coupled with a mass spectrometer (Trace GC Ultra - Thermo Scientific). δD and $\delta^{18}O$ in steam condensates were measured by Liquid Water Isotope Analysis based on Off-Axis Integrated Cavity Output Spectroscopy. All chemical data obtained have analytical uncertainties ≤ 5% for the main gas components and ≤ 10 % for minor and trace gas species.

259 The uncertainties for C, O and H isotopes are ±0.1‰, ±0.05‰ and ±1‰, respectively.
260 The analysis of fumarole gases (including water vapour) permitted to compare their
261 composition with that of local production wells, to discriminate between mantellic and
262 hydrothermal-geothermal origin of the fluids and, finally, to identify the T and P conditions
263 in the geothermal reservoir(s).

264 **3.3. Structural analysis**

265 Structural analysis of the Biancane site has been used to define the fracture network that
266 allows fluid circulation in the shallow portion of the geothermal system. In this work, the
267 term fracture includes any form of discontinuity in the rock, such as faults, joints,
268 deformation bands, cracks, etc.
269 At 46 locations in the Le Biancane area (Fig. 2b) the fractures' and bedding planes' attitudes
270 have been acquired. At 8 locations, out of the 46, oriented pictures were taken for a
271 topological analysis of the fracture network (Fig. 2b).
272 The topology of the fracture network defines how the fractures intersect and it provides an
273 estimate of the fracture network connectivity (Sanderson and Nixon, 2015, 2018). The 2D
274 fracture network representation consists of fracture traces that intersect each other forming
275 fracture segments bounded by nodes (Sanderson and Nixon, 2015; see also Fig. A.1 in
276 Appendix A). A node is the point where a fracture intersects another fracture or the point
277 where the fracture ends. The node can be of three types: i) type I with only one termination
278 (green box in Fig. A.1 in Appendix A), ii) type Y with three terminations (blue box in Fig.
279 A.1), and iii) type X with four terminations (red box in Fig. A.1). The segments defined by
280 nodes are termed branches, while each fracture trace is termed a line. Sanderson and Nixon
281 (2015, 2018) showed that by analysing the types of the nodes (i.e., terminations of the
282 branches) and their relative proportions it is possible to define numerical parameters, such as
283 the number of intersections per line (C_L) and per branch (C_B), that are good proxies for the

degree of the network connectivity. In particular, when C_L>3.57 and C_B>1.56, the fracture network is very well connected (e.g., Balberg et al.,1984; Sanderson and Nixon, 2018). As suggested in Sanderson and Nixon (2018), C_B is a better proxy for the fracture network connectivity than C_L. Moreover, by using the type and the number of nodes it is also possible to derive the probability that a branch (fracture segment) is not connected (PII'), partially connected (PIC') or fully connected to other branches (PCC'). For details, see Appendix A.

4. Results

4.1. Soil CO_2 flux and soil temperature

Measurements of soil CO_2 flux at Le Biancane (197 samples) gave an average value of 188 g m^{-2} day^{-1} and a range of variation of orders of magnitude, from a minimum of 0.04 g m^{-2} day^{-1} to 7252 g m^{-2} day^{-1} (Table 1). The probability plot and the frequency distribution histogram of the soil CO_2 flux measurements (Fig. 3a and 3a') show that their statistical distribution is the result of three combined log-normal populations representing high, low, and very low CO_2 flux populations (HF, LF, VLF, respectively). The CO_2 flux measurements included in the LF and VLF populations represent the larger proportion (85%) of the dataset and gave mean and median values of 21.4 g m^{-2} day^{-1} and 7.1 g m^{-2} day^{-1} (LF) and 1.02 g m^{-2} $day^{-1}$and 0.32 g m^{-2} day^{-1} (VLF), respectively (Table 1). These values fall in the range of the CO_2 flux produced by the biological activity of the soil (0.2-21 g m^{-2} day^{-1}; Cardellini et al., 2003) and are quite low, demonstrating a scarce activity of the local soil characterized by absent or damaged vegetation. The HF population comprises 15% of measurements (30 samples) and returns a mean and median value of 1471 g m^{-2} day^{-1} and 501 g m^{-2} day^{-1}, suggesting the presence of a deep source of CO_2. The large differences between mean and median values highlight that the frequency distributions of the partitioned soil CO_2 flux populations (normally distributed in logarithmic scale) are positively skewed. In the case of skewed distribution with a few

outliers the median is better than the mean for providing values that may be considered as anomalous.

Soil brightness temperatures (146 samples) gave an average value of 34.4 °C and a large range from 18.5 °C to 80.5 °C (Table 1). The temperature measurements are also partitioned into three populations including high, intermediate, and low soil temperatures (HT, IT, LT, Table 1 and Fig. 3b and 3b'). The HT population (with an average of 50 °C) comprises 15% of temperature measurements (22 samples), whereas most of the temperature measurements (70%) fall in the IT population (33 °C on average) and only a few sites show a low soil brightness temperature (15% of measurements with average temperature of 23 °C) mainly located in shaded or vegetated zones at edges of the study area. For the soil brightness temperature mean and median of the partitioned populations are coincident since the relative values are normally distributed.

Examination of Fig. 3a' and 3b' shows that the HF population has a stronger characterization than HT population since the spread of data around the median is smaller than HT, although the relative proportions of the two populations are equal (15%). For this reason, the HF population is clearly recognizable from the adjacent LF population, while the values of the HT population are scattered widely about the median and overlap with the tail of the IT population.

Table 1. Summary statistics for the CO_2 flux, brightness temperature and related partitioned populations. In the columns relative to raw datasets the number of measurements, the mean, the minimum and the maximum of the whole dataset are reported. The proportion (f), the mean and the median of the partitioned populations are reported in the three right columns. Mean and median of the partitioned populations are supported by their two-sided 90% confidence interval (superscript and subscript values).

	Raw dataset		Partitioned populations		
Parameter	# meas. points	Mean [Min-Max] (g m^{-2} day^{-1})	f	Mean (g m^{-2} day^{-1})	Median (g m^{-2} day^{-1})
Soil CO_2 flux	197	188 [0.04 - 7252]	HF 15%	HF 1472^{3985}_{845}	HF 501^{1358}_{288}
			LF 80%	LF $21.5^{31.9}_{15.9}$	LF $7.1^{10.5}_{5.2}$

			VLF 5%	VLF $1.02^{18.9}_{0.41}$ VLF $0.32^{5.83}_{0.13}$
	# meas. points	Mean[Min-Max] (°C)		Mean =Median (°C)
Soil brightness T	146	34.4 [18.5 - 80.5]	HF 15%	HT 50±5.0
			LF 70%	IT 33±1.3
			VLF 15%	LT 23±0.7

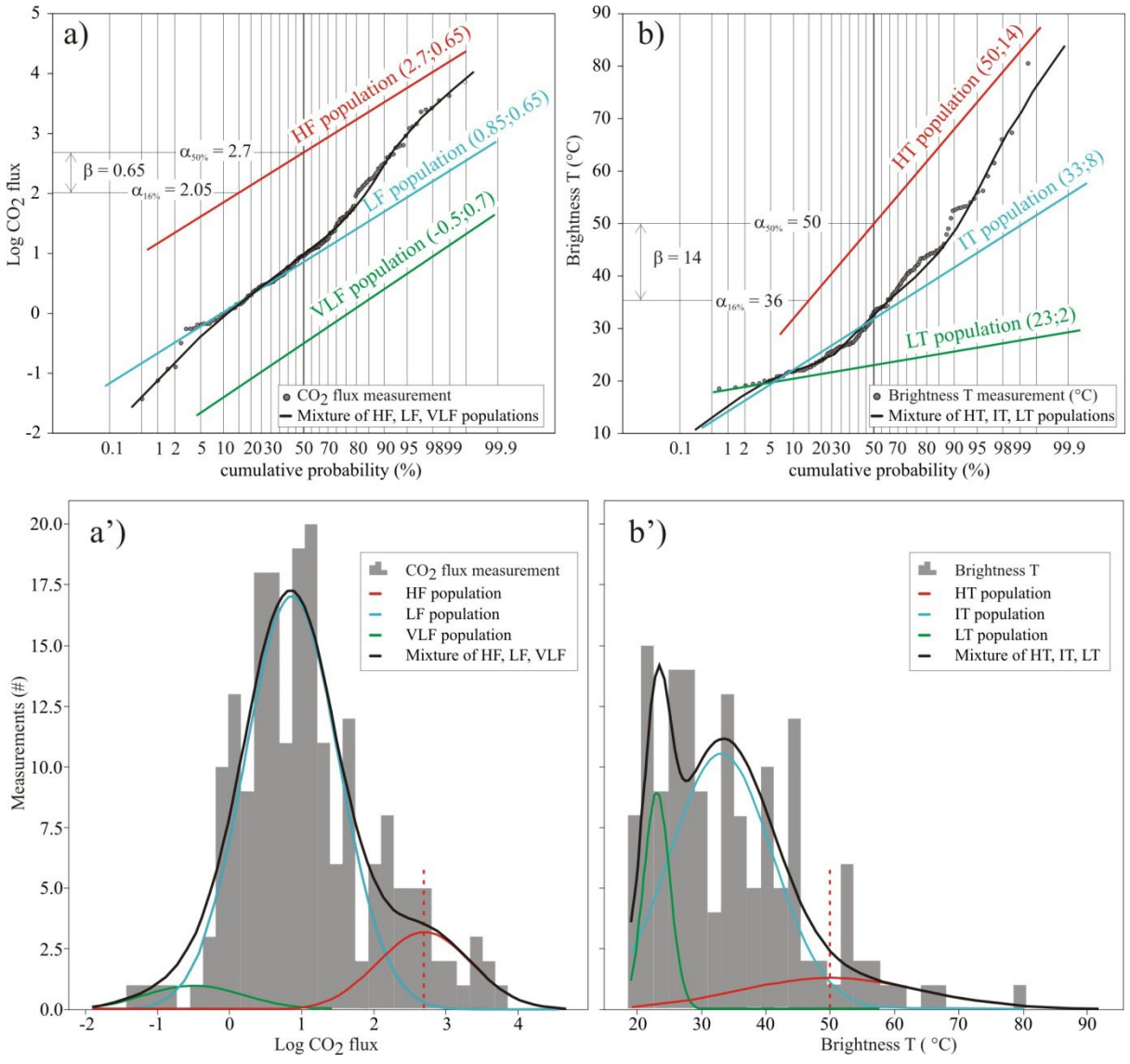

Figure 3. Probability plot of a) soil CO_2 flux (Log scale) and b) soil brightness temperature measurements. Both parameters have polymodal distributions resulting in the mixture of 3 individual populations (black curves). Each population plots as a straight line (coloured lines). The intercept of each partitioned population with the 50% line (marked vertical line)

342 gives the median of the population ($\alpha_{50\%}$), while its standard deviations (β) can be read as the
343 difference associated to the interval 16% to 50% (or 50% to 84%). The derivation of these
344 parameters is shown, as an example, for the HF population in a) and for the HT population in
345 b). The mean and the standard deviation of the partitioned populations are reported in
346 brackets. Frequency distribution histograms of soil CO_2 flux (Log scale) and soil brightness
347 temperature measurements are shown in a') and b'), respectively. The partitioned populations
348 are drawn by using a Gaussian with the derived median and standard deviation. Vertical
349 dashed red lines identify the median of the HF and HT populations. In a') and b') the black
350 curves are the resulting theoretical distributions of the mixture of the partitioned populations
351 for the soil CO_2 flux and soil brightness temperature, respectively. See the text for further
352 details.
353
354 The maps of the soil CO_2 flux and soil brightness temperature, returned by the sGs procedure,
355 are shown in Fig.s 4a,b. A total CO_2 output of 11.5±0.77 t day^{-1} was estimated for the
356 investigated area of about 60,000 m^2. Main degassing areas define some spots in the central
357 and NE sector of the study area (Fig. 4a) roughly distributed along a NE-SW band, a
358 direction coincident with the orientation of the faults bordering Le Biancane area (Fig. 1c).
359 These degassing areas were identified as having hot ground by the mapping of the soil
360 brightness temperature (Fig. 4b). In particular, the main CO_2 soil flux anomaly (with values
361 exceeding the median value of the HF population, see Fig. 4a) falls in the sector of the B8
362 fumarole (Fig. 2a) where measured temperatures as hot as 50 °C occur (i.e., temperatures
363 higher than the median value of the HT population).

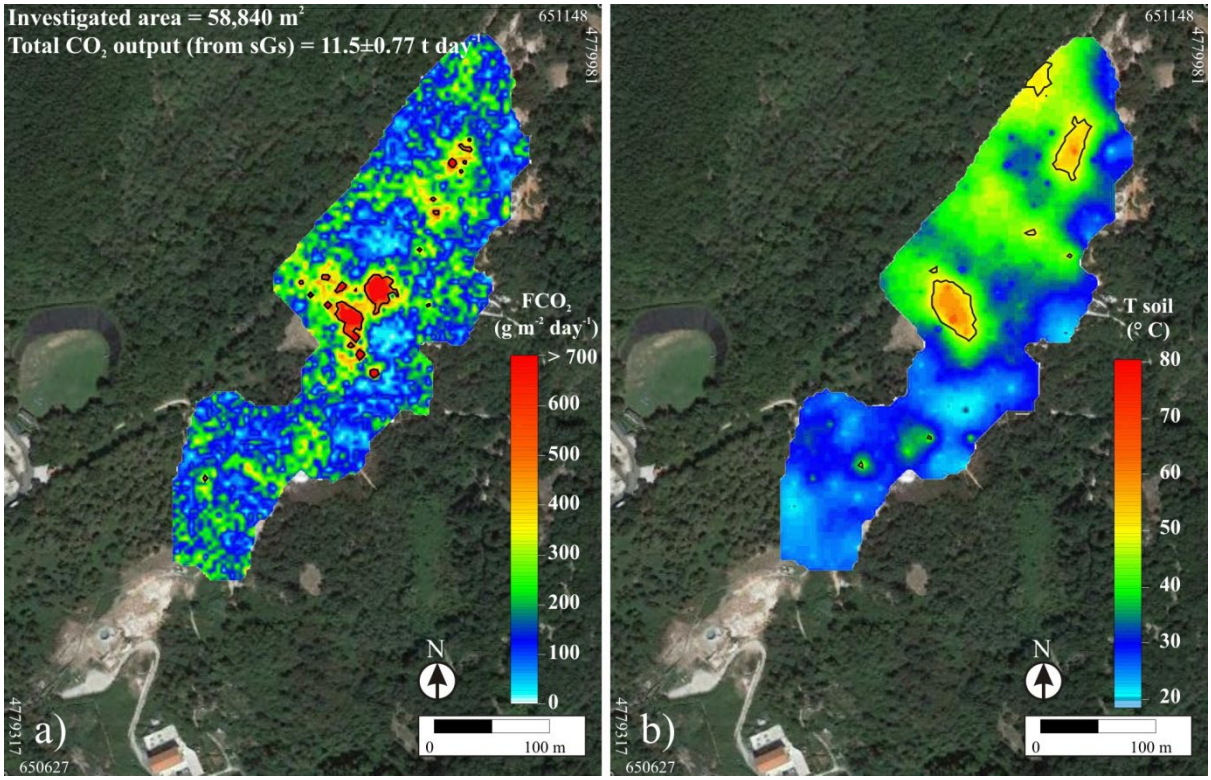

Figure 4. Maps of the sGs results for a) Soil CO_2 flux and b) Soil brightness temperature. The black outlines in both maps enclose regions of the respective HF and HT populations, namely where soil CO_2 flux > 501 g m^{-2} day^{-1} and soil brightness temperature > 50 °C. In a) the total soil CO_2 output is indicated together with the extension of the investigated area.

4.2. Gas geochemistry

We present here the chemical and isotopic compositions of the fumaroles sampled at Le Biancane in June 2021, together with unpublished data of other local fumaroles sampled and analyzed in 2005-2006 by a subset of the authors of this study. For comparison, we also considered the chemical composition of local fumaroles and geothermal production wells reported in Chiodini et al. (1991), Chiodini and Marini (1998) and Menichini (2006). Most of these samples fall in the neighbourhood of Le Biancane, but unfortunately the authors do not indicate their precise locations.

Fumarole samples contain more than 98-99% (mol) water, and on a water-free basis, CO_2, H_2, CH_4 and H_2S are the most abundant gas components (Table 1 in supplementary material). The gases from the fumaroles have a similar chemical composition of those found in the

geothermal production wells (Table 1 in supplementary material).

B6 and B7 fumaroles are located in the SW side of Le Biancane area (see location in Fig. 2a) and discharge superheated vapour with temperature of 110.5 °C and 115.3 °C, respectively. Such high values seem to characterize only this portion of Le Biancane. In the central sector of the investigated area (characterized by higher morphological elevation) the B8 fumarole shows a discharge temperature of 99 °C. It is interesting to note that the B6 fumarole sample of July 2006 recorded a high temperature of 129.4 °C (Table 1 in supplementary material). Similar temperature trends were also recorded in some shallow production wells located around this area (Enel Green Power, 2022, personal communication).

Other natural gas manifestations sampled in 2005-2006 inside Le Biancane area (i.e., B1, B2, B3, B4, in Fig. 2a) and abroad (i.e., LS1, SP1, SP2, V1, V2, V3, inset of Fig. 2a) showed outlet temperatures close or very close to the water boiling point at the local atmospheric pressure conditions (Table 1 in supplementary material), some of them were characterized by low flow. This indicates that the condensation near surface level could affect some of the collected gases.

In the triangular CO_2-N_2-Ar diagram (Fig. 5a) all collected samples plot inside the compositional triangle mantle-air-air saturated water (ASW), suggesting mixing between these three end members, with the prevalence of the mantle component. Exceptions are two fumaroles located about 500 m N of Le Biancane (i.e., V1 and V3, Fig. 2a) which are characterized by different N_2/Ar ratio and the B2 fumarole, inside Le Biancane, showing higher contents of air along the mantle-air mixing line. Using gas species less affected by steam separation and/or condensation processes, the triangular CH_4-CO-H_2 diagram (Fig. 5b) allows discrimination between high temperature volcanic gases and hydrothermal-geothermal gases (Chiodini et al., 1992). As expected, all collected gas samples plot close to the CH_4-vertex (e.g., hydrothermal-geothermal gases), in very good agreement with gas samples

collected from LTGF wells.

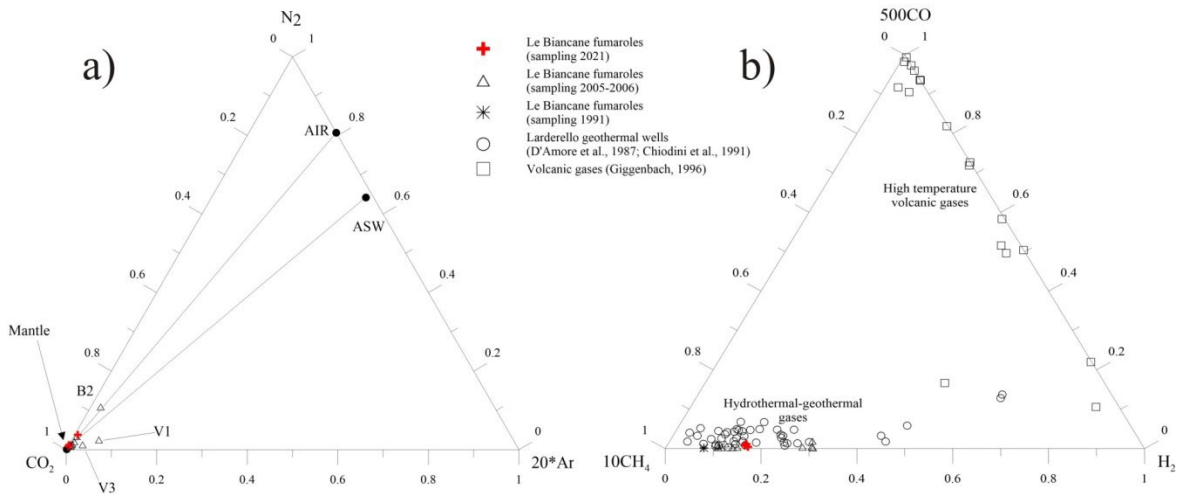

Figure 5. Ternary plots of Le Biancane gases. a) CO_2-Ar-N_2 plot. The compositions of mantle, air and air saturated water (ASW) are also reported. b) CH_4-H_2-CO plot. Open circles are geothermal wells of the LTGF (data from D'Amore et al., 1987 and Chiodini et al., 1991). The field of typical volcanic gases is also shown (data from Giggenbach, 1996).

Using the approach described in Bertrami et al. (1985), the equilibrium between gas species in geothermal fluids discharged by fumaroles and production wells was evaluated, considering the system H_2O-CO_2-CH_4-H_2-CO. The following independent reactions were considered:

$$CO_2 + H_2 = CO + H_2O_{(gas)} \quad (1)$$

$$CH_4 + 3CO_2 = 4CO + 2H_2O_{(liquid)} \quad (2)$$

assuming that water partial pressure is controlled by the presence of liquid water. This hypothesis is valid also for vapour-dominated geothermal systems, according to accepted models (e.g., Truesdell and White, 1973).

The equilibrium constants of reactions (1) and (2) can be written as follows, considering the distribution of gas species between gas and liquid phase:

$$K1 = \frac{X_{H2O} \cdot X_{CO}}{(1 - X_{H2O}) \cdot X_{CO} \cdot X_{H2}} \cdot \frac{(y + \frac{1-y}{B_{CO2}}) \cdot (y + \frac{1-y}{B_{H2}})}{(y + \frac{1-y}{B_{CO}})} \quad (3)$$

$$K2 = \frac{X_{CO}^4}{X_{CO2}^3 \cdot X_{CH4}} \cdot \frac{(y + \frac{1-y}{B_{CO2}})^3 \cdot (y + \frac{1-y}{B_{H2}})}{(y + \frac{1-y}{B_{CO}})^4} \quad (4)$$

where B_i represent the distribution coefficient for component i between vapour and liquid phase, X_{H2O} is the molar fraction of the water in the total fluid, X_i is the molar fraction of the component i in the non-condensable fraction and y is the steam/liquid ratio in the equilibration zone (y=1 means only steam is present at depth). Both equilibrium constants are influenced by the steam/liquid ratio but, as suggested by Bertrami et al. (1985), the influence on equation (4) is smaller.

The functions describing the correlation from temperature of the vapour-liquid distribution coefficient B_i in the range 100-340 °C are given by Giggenbach (1980) for CO_2, CH_4 and H_2, and Bertrami et al. (1985) for CO:

$$\log B_{CO2} = 4.7593 - 0.01092 \cdot T_{(°C)}$$

$$\log B_{CH4} = 6.0783 - 0.01383 \cdot T_{(°C)}$$

$$\log B_{H2} = 6.2283 - 0.01403 \cdot T_{(°C)}$$

$$\log B_{CO} = 6.3173 - 0.01388 \cdot T_{(°C)}$$

On the basis of thermodynamic data from Barin and Knacke (1973) the following equations were obtained:

$$\log K1 = 1.9363 - \frac{2001.65}{(T_{°C} + 273.15)} \quad (5)$$

$$\log K2 = 8.0651 - \frac{13605.63}{(T_{°C} + 273.15)} \quad (6)$$

Equations (5) and (6) were used to calculate the temperature and steam /liquid ratio in the gas equilibration zone. Because equation (4) is practically independent from the steam/liquid

ratio, at least for y>0.05 (Bertrami et al., 1985), only the temperatures calculated for the system H_2O-CO_2-H_2-CH_4-CO were considered (GCT in Table 1 in supplementary material). The estimation of the equilibrium temperatures for the local fumaroles (Fig. 6 and Table 1 in supplementary material) ranges from 202 °C (B8 fumarole) to a maximum value of 238 °C (B7 fumarole and B6 fumarole in 2006), in agreement with the temperatures measured in the Larderello geothermal system (Bertrami et al., 1985; Bertani et al., 2005). Fumarole samples possibly affected by condensation have been omitted from Figure 6. In general, the fumaroles of Le Biancane and surrounding area show the same pattern indicated by the fluids discharged by geothermal wells, suggesting common sources and evolution trends of gases. Assuming that fugacity of water pressure corresponds to water saturation pressure, the following function for pure water can be used to estimate P_{H2O} (Table 1 in supplementary material):

$$\log P_{H2O} = 5.51 - \frac{2048}{(T_{\circ C}+273.15)} \quad (7)$$

For the June 2021 samples, P_{H2O} ranged from 15.8 bar (B8 fumarole) to 31.9 bar (B7 fumarole), in very good agreement with estimates for geothermal wells and other local fumaroles sampled in different years (Table 1 in supplementary material). Using the equilibrium constant (equation 3) of the reaction (1), the water saturation pressure previously calculated has been used to obtain P_{CO2} by means of the following equation (Chiodini and Cioni, 1989):

$$\log P_{CO2} = 3.573 - \left(\frac{46}{(T_{\circ C}+273.15)}\right) - \log \frac{H_2}{CO} \quad (8)$$

The results indicate P_{CO2} values of a few tenths of bar calculated for natural gas emissions collected in June 2021 (from 0.15 bar of B8 fumarole to 0.42 bar of B7 fumarole), which are

in agreement with the values of some geothermal wells (Chiodini et al., 1991).

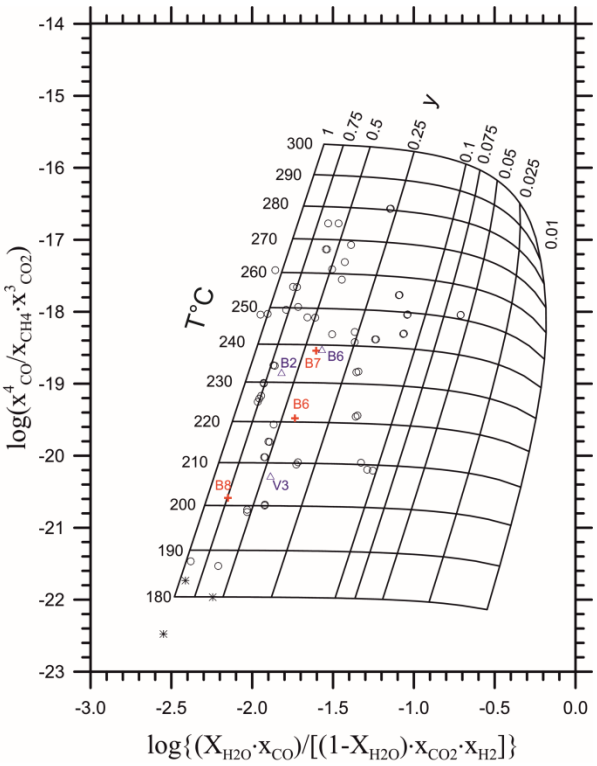

Figure 6. Plot $\log[X^4_{CO}/(X_{CH4}\cdot X^3_{CO2})]$ vs. $\log[(X_{H2O}\cdot X_{CO})/(1-X_{H2O})\cdot X_{CO2}\cdot X_{H2})]$. X_{H2O} refers to water molar fraction on total fluids, whereas X_{CO}, X_{CH4} and X_{CO2} represent molar fraction of components in non-condensable fraction (from Bertrami et al., 1985, modified). The steam/liquid ratio is indicated with *y*. Symbols of the samples as in Fig. 5.

Chiodini et al. (1991) showed that also the H_2S/COS ratio can be used to evaluate P_{CO2} in the gas equilibration zone, obtaining results comparable with those derived from the H_2/CO ratio. These authors proposed the following gas reactions:

$$CO_2 + H_2S = COS + H_2O \quad (9)$$

$$CO + H_2S = COS + H_2 \quad (10)$$

to derive the P_{CO2} based on the H_2S/COS ratio, using the equilibration temperature of fluids calculated by the geothermometric expression of Bertrami et al. (1985) and considering the equilibrium conditions attained in a pure vapour phase. It is worth highlighting that the study

of Chiodini et al. (1991) is built on the COS content and COS/CO_2 ratios measured in geothermal fluids of 12 production wells of the Larderello field. Because of the analytical difficulties to detect COS in natural fluids, this approach has not led to any other application, although it was very promising.

In this study we set up a suitable analytical procedure to detect all the components involved in the two gas reactions above mentioned (Eq.s 9 and 10), and we were able to detect, for the first time in natural geothermal manifestations, the COS content with reliable accuracy and precision. The derived P_{CO2} values for the three fumaroles of le Biancane sampled in June 2021 are of the same magnitude (a few tenths of bar) of those calculated by the H_2/CO ratio (see Table 1 in supplementary material). Moreover, their compositions show a similar pattern associated to the fluids of the geothermal wells, approaching the theoretical equilibration vapour phase curve calculated at a temperature of 200 °C (Fig.7).

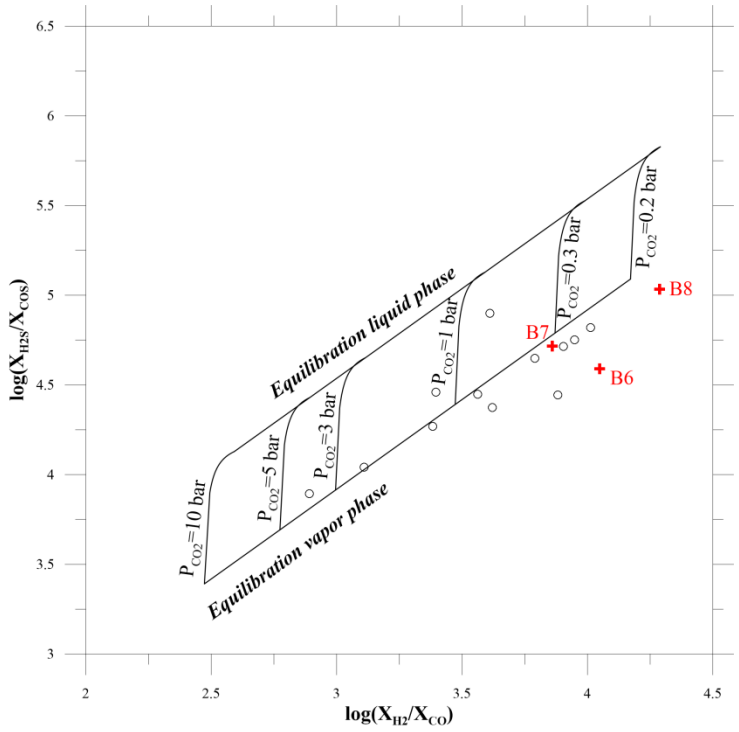

Figure 7. Plot log (X_{H2S}/X_{COS}) vs. log (X_{H2}/X_{CO}) (from Chiodini and al., 1991, modified). The theoretical ratios for vapour and liquid phase at different P_{CO2} and at T= 200 °C are also reported as equilibration vapour phase and equilibration liquid phase lines, respectively.

503 Available data from Larderello geothermal wells are included (Chiodini et al., 1991).
504 Symbols of the samples as in Fig. 5.

505 The isotopic composition of $\delta^{13}C_{(CO2)}$ in LTGF gas samples ranges from -2.35 to -4.19‰
506 (Table 1 in supplementary material) in very good agreement with isotope data of geothermal
507 wells drilled in the sedimentary carbonate shallow geothermal reservoir, which are
508 characterized by values ranging from -2.80 to -5.9‰ (Gherardi et al., 2005). This finding
509 suggests that the carbonate-evaporite sedimentary formation of the Tuscan Nappe,
510 outcropping in Le Biancane area, is the main source of CO_2, though minor contributions of
511 magmatic CO_2 (typical range from -3 to -8‰) cannot be ruled out.
512 Oxygen and hydrogen isotope analyses were performed on steam condensate samples. As
513 shown in Table 1 (supplementary material), super-heated B6 and B7 fumaroles have $\delta^{18}O$ = -
514 3.63‰ and -3.83‰, respectively, and δD = -36.2‰ and -36.4‰, respectively, whereas the
515 B8 fumarole (with discharge temperature of 99 °C) has isotope composition of $\delta^{18}O$ = -
516 5.01‰ and δD = -44.3‰. These values are reported in the classical $\delta^{18}O$‰ vs δD‰
517 correlation diagram (Fig. 8), together with data for local cold and thermal springs (Panichi et
518 al., 1974) and condensed steam from geothermal wells tapping the shallower reservoir
519 collected before (sampling data 1964-1969, Panichi et al., 1974) and after water re-injection
520 (sampling date 1986, Bolognesi, 2011). The isotopic composition of local re-injected water
521 (D'Amore et al., 1987; Cappetti et al., 1995; Panichi et al., 1995) and the field of the primary
522 steam (Cappetti et al., 1995; Bolognesi, 2011) are also shown. For reference, the Water
523 Meteoric Water Line (WMWL, Craig, 1961) and Central Mediterranean Meteoric Water Line
524 (CMMWL, Gat and Carmi, 1970) are also plotted. In Figure 8 the steam condensates from
525 geothermal wells collected before re-injection (open circles) show a horizontal displacement
526 characterized by large variations in $\delta^{18}O$ (-5.5/+0.5‰). As mentioned in Panichi et al. (1974),
527 the water-rock interaction process between water and oxygenated rocks (as limestone and/or

528 silicates) can explain such an oxygen shift toward higher values, even if different $\delta^{18}O$
529 enrichments noted in some areas could reflect other processes (i.e., complex deep circulation
530 pattern and/or different thermal conditions). The alignment of the data before re-injection
531 points towards the isotopic compositions of cold and thermal waters and fits with the
532 hypothesised isotope composition for the local natural recharge (Panichi et al., 1974; 1995).
533 Mixing processes between surface meteoric waters and deep fluids occurring in the shallow
534 reservoirs may also explain this distribution. Starting from the composition of the primary
535 steam hypothesised in Larderello (Cappetti et al., 1995; Bolognesi, 2011), the samples of the
536 geothermal wells collected in 1986 (i.e., after re-injection) clearly show the influence of the
537 local re-injected water (Fig. 8). Steam condensates from natural gas emissions sampled in
538 June 2021 show different distributions. In particular, superheated fumaroles (samples B6 and
539 B7) show δD values significantly more positive than those typical for the primary steam and
540 geothermal wells collected before re-injection. Their values seem to be consistent with those
541 for geothermal wells affected by re-injection, even if δD values up to -35‰ are sometimes
542 found in some geothermal wells in the area, which are not affected by re-injection (Enel
543 Green Power, 2022 personal communication). Very different behaviour is shown by the
544 sample B8, which shows a more negative δD composition, in agreement with those found for
545 geothermal wells before re-injection and therefore also with the primary steam and local
546 springs.
547 Helium isotopic compositions for natural gas manifestations are available only for samples
548 collected in 2005-2006 (Menichini, 2006). The R/R_a ratio (where R is the $^3He/^4He$ ratio of the
549 sample and R_a that of the air, $1.4*10^{-6}$) ranges from 1.88 to 2.19 in agreement with several
550 data obtained from geothermal wells in the Larderello geothermal system and characterized
551 by values from 0.5 to 3.2 (Torgersen, 1980; Hooker et al., 1985; Magro et al., 2003; Gherardi
552 et al., 2005). This suggests a common source of helium between geothermal wells and natural

manifestations, despite data of He/Ne ratio is lacking for fumarole samples to evaluate the atmospheric contribution of He in collected samples. However, the low abundances of atmospheric components measured in fumarole samples allow us to exclude significant air-contamination.

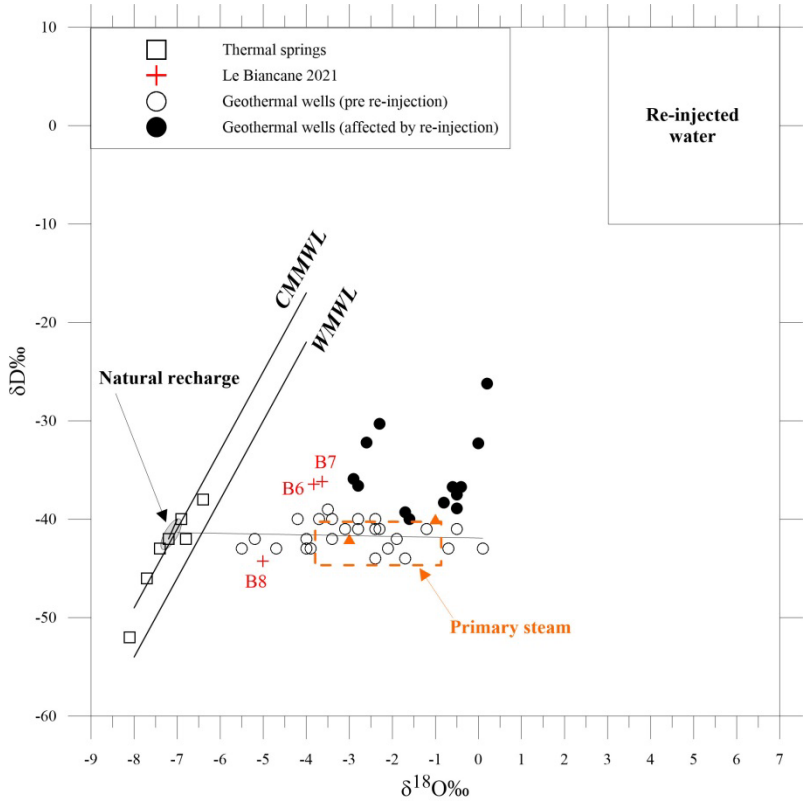

Figure 8. δD and $\delta^{18}O$ values from fumarole samples collected in Le Biancane area are compared with those of geothermal wells sampled before and after water re-injection, primary steam, local re-injected water and local cold and thermal springs. The World Meteoric Water Line (WMWL) and the Central Mediterranean Meteoric Water Line (CMMWL) are also shown.

4.3. Structural analysis

The results of the structural analysis show that NW-SE and NE-SW trending fractures are the most frequent in Le Biancane area (Fig. 9a) while the bedding planes show a (less evident) prevalent NE-SW orientation (Fig. 9b). Measured fractures are mostly steeply dipping while bedding planes show a low-medium dip (Fig. 9c). As such, the fracture systems are coherent

568 with a general E-W extension (direction of the least principal stress, Fig. 9a) typical of the
569 Italian Apennines.

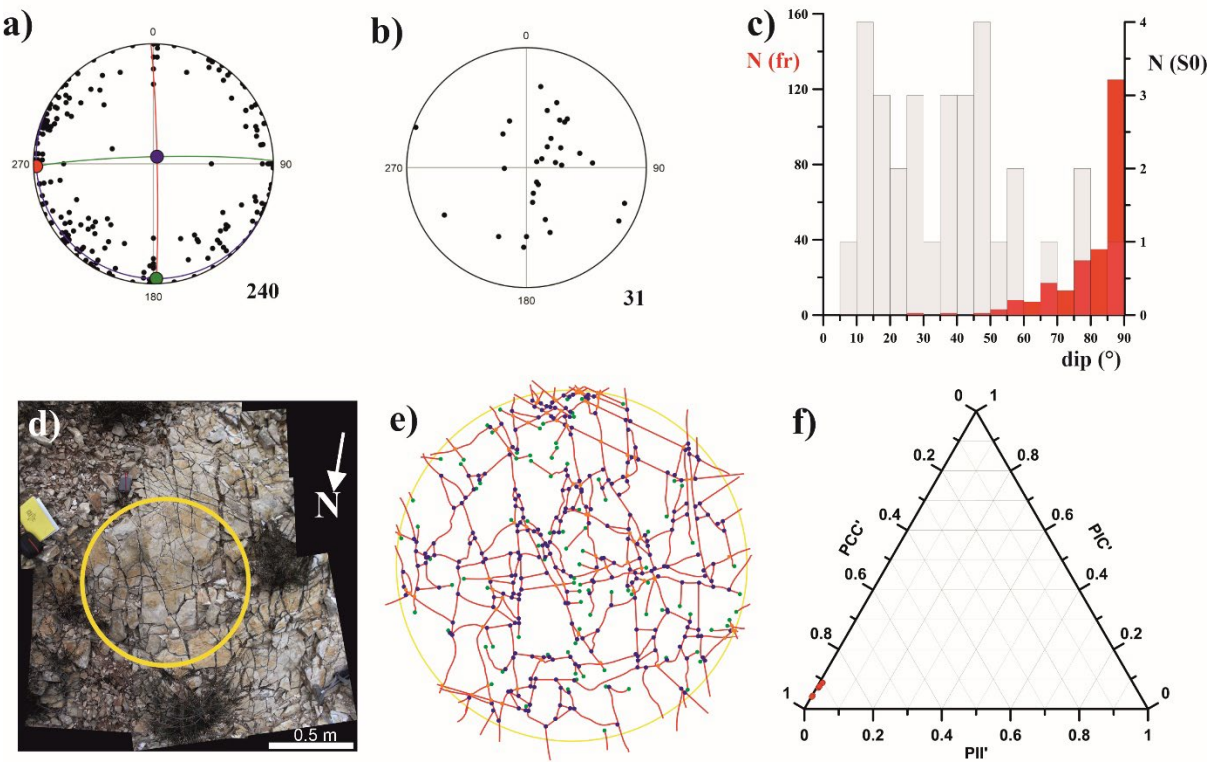

570

571 **Figure 9.** a) Stereo net (lower hemisphere) of the poles to fractures; red circle: sigma3, green
572 circle: sigma2, blue circle: sigma1. b) Stereo net (lower hemisphere) of the poles to bedding
573 (S0). c) Histogram (5° bin) of the dip of bedding (N(S0), grey bars) and of fractures (N(fr),
574 red bars). d) Picture of the fracture network in the site x4 (Fig. 2b), the yellow circle (1 m in
575 diameter) is used for the topological analysis. e) Fracture network mapping (as in Sanderson
576 and Nixon, 2015) with nodes (green circle: node I; blue circle: node Y; orange circle: node X;
577 see Appendix A). f) Ternary plot of connectivity (low connectivity, PII', intermediate
578 connectivity, PIC' and high connectivity, PCC') for eight sites located at Le Biancane (Fig.
579 2b), all falling in the field of high connectivity (red dots). For details see Appendix A.

580 The topological analysis of the fracture network was performed through the analysis of eight
581 pictures (one of them in Fig. 9d), used to determine the number and the typology of the nodes
582 of the discontinuity network in circular sectors with 1 m diameter (Fig. 9e). Results indicate
583 that all the fracture networks are topologically very well connected with high PCC' values

584 (red dots in Fig. 9f). Similar indications come from the values of C_L and C_B parameters
585 (Table 2) that confirm the attitude to the connectivity of the fracture network.

586 Table 2. Values of the C_L and C_B parameters from the topological analysis of the fracture
587 network at Le Biancane.

Site	X (UTM_WGS84)	Y (UTM_WGS84)	C_L	C_B
x0	650931	4779726	3.688	1.821
x3	650961	4779750	3.914	1.854
x4	650976	4779817	4.474	1.91
x5	651025	4779902	4.147	1.857
x6	650964	4779720	3.53	1.826
x8	650888	4779603	3.582	1.848
x9	650789	4779548	3.808	1.847
x10	651063	4779934	4.64	1.918

588
589 **5. Interpretation of results and discussion**

590 In the site of Le Biancane the total CO_2 flux normalized by surveyed area is at a low level
591 (0.195 kg m^{-2} day^{-1}) if compared to those measured in other degassing areas (volcanic,
592 geothermal or tectonically active) of southern and central Italy (Fig. 10). The value derived
593 by our investigation is strikingly similar to the CO_2 output reported in the work of Cabassi et
594 al. (2021). They computed a total CO_2 output of 3.15 t day^{-1} over an area of about 20,000 m^2
595 in the SW sector of Le Biancane, then a normalized flux of 0.157 kg m^{-2} day^{-1}. Since the area
596 investigated in this study is adjacent to, or partially overlapping, the sector quoted above, we
597 argue that part of this difference could be due to the different approaches used to calculate the
598 total CO_2 output. Cabassi et al. (2021) used the Graphical Statistical Analysis, according to
599 the procedure proposed by Sinclair (1974), whereas we applied the sequential Gaussian
600 simulation approach, as reported in Cardellini et al. (2003).

The peculiarity of this site is that the amount of CO_2 is not released uniformly from the whole "bare" area, but rather from relatively small portions. In our investigation, some spots located in the central and in the NE sectors of the surveyed area (Fig. 4a) contribute more than 11% to the total output (1.23 t day^{-1} vs 11.5 t day^{-1}), despite the observation that their areal extent is only 2.5% of the total area (1408 m^2 out of 58,840 m^2).

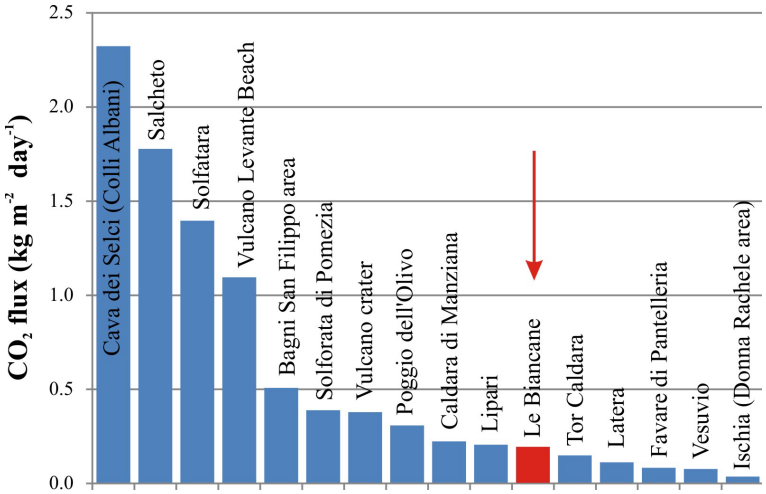

Figure 10. Histogram of the CO_2 flux from sixteen degassing areas of the Italian territory (data from Tarchini et al., 2022) compared with the CO_2 output of Le Biancane (this work).

These sectors are likely characterized by high vertical permeability, with fracture networks vertically very well connected. The fractures are mainly NW-SE and NE-SW orientated and with steep dips, providing preferential pathways for non-condensable gases (mainly CO_2) and heat to escape to the surface. The general attitude to the "transport" of this fracture system is supported by the deep roots of the tectonic structures, as revealed by a 3D seismic survey performed at Travale in 2003 (Casini et al., 2010).

The spatial pattern produced by elevated CO_2 flux areas is comparable with that produced by soil brightness temperature anomalies (Fig.s 4a,b). The overall correlation between CO_2 flux measurements and soil brightness temperature increases for high values of CO_2 flux and brightness temperature, i.e. for samples falling in the HF and the HT populations. In Fig. 11a, the correlations among all measures are displayed, with their quadratic fit and asymmetric

standard deviation. The plot confirms that the correlations improve when soil temperatures are higher than 55 °C (corresponding to high CO_2 fluxes), while colder values are too scattered to produce a meaningful relationship. This behaviour is partly due to the heating of the ground by solar radiation during the field work. The high-flux/high-temperature correlation also arises by the inspection of Fig. 11b, where the red area includes pixels where the soil CO_2 flux and the soil temperature are simultaneously above the median value of the HF and HT populations, respectively. Common red peak area is 544 m^2, with a fitting index equal to 0.16, where the fitting index is defined as the ratio of the intersection of the "anomalous" regions divided by their union (Jaccard, 1901; Granieri et al., 2018). The closer the fitting index is to 1, the larger is the similarity of the extreme value regions of the two variables. Ultimately, the highly degassing area displays soil temperature as high as 50 °C and includes the B8 fumarole at discharge temperature of 99 °C (Fig. 11b).

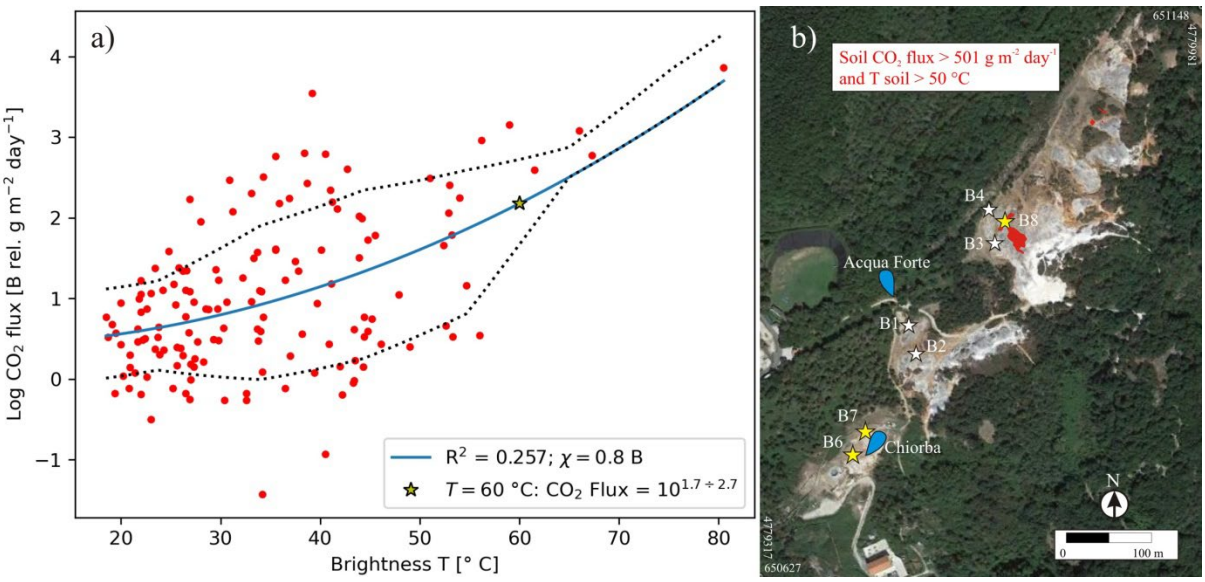

Figure 11. a) Comparison between the soil brightness temperature and the Log CO_2 flux measured in the same locations. The blue line is a quadratic fit of all the data, with global Pearson's χ = 0.8 Bel relative to 1 g m^{-2} day^{-1}, and coefficient of determination R^2 = 0.26. The Bel is the standard to express the ratio of a quantity with respect to a reference in logarithmic scale with base 10. In b) the common area where simultaneously the soil CO_2 flux and the soil temperature are above the median value of their HF (501 g m^{-2} day^{-1}) and

643 HT (50 °C) populations is shown.
644
645 The natural gas manifestations of Le Biancane display different chemical and isotopic
646 composition depending on their location. In the SW sector there are superheated fumaroles
647 (B6 and B7 fumaroles) with geochemical characterization similar to those of geothermal
648 wells located at some distance from Le Biancane, whereas fumaroles in the central sector
649 (B3, B4, B8) are quite similar to geothermal wells close to Le Biancane area. This could
650 suggest the pivotal role played by the fracture network in enhancing the secondary
651 permeability of the shallow reservoir, thus allowing geothermal fluids to maintain the
652 equilibrium state recorded at depth with a different degree during the movement toward the
653 surface. Moreover, these preferential pathways for the gas could become blocked over time
654 by mineral precipitation or formation of clays into the fractures and then migrate elsewhere,
655 also on a small scale. In addition, chemical and isotopic differences in gas composition could
656 arise from different relations between rising fluids, infiltrating meteoric waters and, possibly,
657 for re-injected spent steam. In our opinion, more data of production geothermal wells and
658 natural manifestations are required for better understanding these aspects.
659 The H_2O/CO_2 ratio is typically high for the three fumaroles (B6, B7, and B8) sampled during
660 the June 2021 survey, ranging from 56 to 84 by weight, with an average value of 71. High
661 values are also confirmed by fumarole samples collected in 1991 and 2005-2006 (see Table 1
662 in supplementary material). Assuming the measured H_2O/CO_2 values as representative of the
663 primary fluid feeding the local natural manifestations, we estimated a total amount of vapour
664 of 970, 852 and 649 t day^{-1} for B6, B7 and B8, respectively, associated with the measured
665 CO_2 output of 11.5 t day^{-1}. This vapour forms at temperatures between 202 °C and 238 °C,
666 assuming gas equilibria in the H_2O-CO_2-CH_4-H_2-CO system, with relative equilibrium P_{H2O}
667 ranging between 15.8 and 31.9 bar, assuming that water partial pressure is controlled by the
668 presence of liquid water (Eq. 9). In the reservoir, P_{CO2} ranges between 0.15 and 0.42 bar,

669 based on the fumarole H_2/CO ratio (Eq. 10) and confirmed by the equilibrium in the H_2S-
670 COS-H_2-CO system.
671 When the vapour rises from depth, it condenses and produces a liquid phase that remains
672 confined within the reservoir because of the impermeable covering, whereas CO_2, which is
673 non-condensable gas, is discharged almost entirely at the soil surface. In the area of Le
674 Biancane, since the covering is absent, most of the condensate flows to the surface, feeding
675 the local springs (Chiorba and Acqua Forte, see Fig. 2a for their location) where $CaSO_4$
676 waters with pH=6.4-6.5 are predominant (Ceccarelli et al., 1987). During our investigation in
677 May-June 2021, there was no evidence of visible steaming ground (that is, the soil was
678 generally dry) except for very limited sectors around the main fractures where soil
679 temperatures > 70 °C were recorded.
680 The movement of H_2O (vapour) and CO_2 from depth, as well as the steam condensation at
681 near surface conditions, transfer efficacy energy toward the soil. Following the definition of
682 Hochstein and Bromley (2005), we used the term 'vapour' to refer "*to the gas phase of water*
683 *without condensation that exists strictly below the ground surface, whereas 'steam' is vapour*
684 *with minor condensation that occurs in the air and at the near-surface layer"*. The heat
685 transported by the H_2O is the sum of three processes (Chiodini et al., 2001), the first one
686 (process a) associated with the vapour moving from reservoir conditions (T= 202-238 °C,
687 P_{H2O}=15.8-31.9 bar) to the condensation layer (T=100 °C and P_{H2O}= 0.99 bar), the second one
688 (process b) associated to the steam condensation at T=100 °C (assuming the enthalpy of
689 evaporation equals to 2257 kJ kg^{-1}, Keenan et al., 1969) and the third (process c) associated
690 to the cooling of the condensate (i.e., H_2O_{liquid}) from 100°C to the local seasonal value of 20
691 °C. The heat transported by the non-condensable CO_2 is instead due to the gas movement
692 (process d) from T and P conditions of the reservoir (T= 202-238 °C, P_{CO2}=0.15-0.42 bar) to
693 the atmosphere (T=20 °C and P_{CO2}= 400 ppm or 0.0004 bar). Assuming the vapour and the

694 CO_2 mass flux aforementioned, the estimates of the energy associated to each process were
695 calculated by using the National Institute of Standards and Technology Chemistry WebBook
696 (Lemmon et al. NIST SRD 69):
697
698 $Q_a = 7.82\ x\ 10^{10}$ J day^{-1} (or 0.906 MW) - $1.25\ x\ 10^{11}$ J day^{-1} (or 1.45 MW) for T=202 °C
699 and P_{H2O}=15.8 bar and T=238 °C and P_{H2O}=31.9 bar, respectively;
700 $Q_b = 1.46\ x\ 10^{12}$ J day^{-1} (or 16.9 MW) - $2.19\ x\ 10^{12}$ J day^{-1} (or 25.3 MW);
701 $Q_c = 2.17\ x\ 10^{11}$ J day^{-1} (or 2.51 MW) - $3.24\ x\ 10^{11}$ J day^{-1} (or 3.76 MW);
702 $Q_d = 1.94\ x\ 10^{9}$ J day^{-1} (or 0.0225 MW) - $2.36\ x\ 10^{9}$ J day^{-1} (or 0.0236 MW) for T=202 °C
703 and P_{CO2}=0.15 bar and T=238 °C and P_{CO2}=0.42 bar, respectively;
704
705 where Q_a, Q_b, Q_c, and Q_d are the heat quantities associated with the a, b, c and d processes
706 described above. Then, the total thermal energy associated with the natural emissions of Le
707 Biancane ranges from 1.76 x 10^{12} J day^{-1} (or 20.4 MW) to 2.64 x 10^{12} J day^{-1} (30.6 MW),
708 most of it (about 99.9%) transported by the H_2O. The equivalent specific heat flux (i.e., the
709 total heat flux normalized by surveyed area) ranges from 255 to 382 W m^{-2}, assuming an
710 emissive area of 80,000 m^2. This value is relatively high if compared with the thermal
711 emission from some volcanic areas characterized by extensive degassing ground (e.g., 50-60
712 W m^{-2} at the crater of Vesuvio, Vulcano and Nisyros (Chiodini et al., 2005)), but not too
713 different from the value found for the Solfatara (224 W m^{-2}, Chiodini et al., 2001), and
714 strikingly comparable with the values found by Hochstein and Bromley (2005) in the similar
715 geothermal system of Wairakei (New Zealand) where specific conductive heat flux of several
716 hundred W m^{-2} (with a maximum of 566 W m^{-2}) were computed. The results from our
717 geochemical and structural studies allowed us to integrate the general sketch proposed by

718 Hurvitz et al., (2012) for a vapour-dominant type geothermal field with mass and energy
719 fluxes typical for LTGF. Figure 12 summarizes the findings of this study.
720

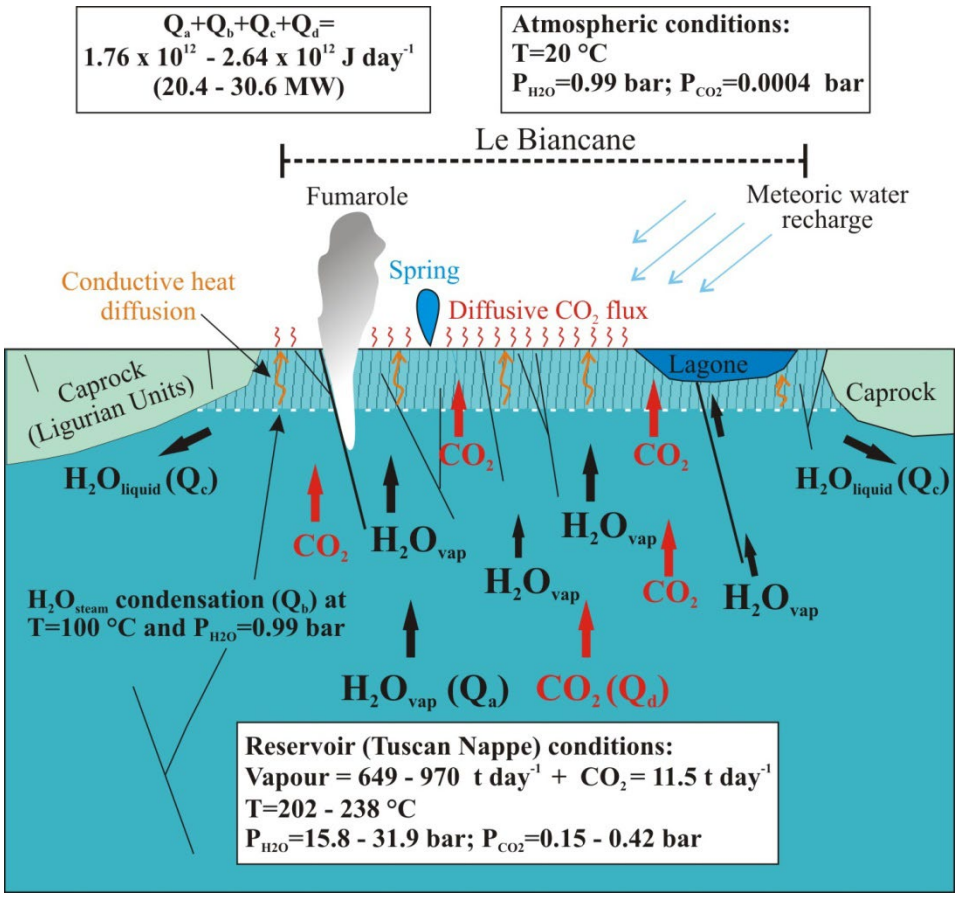

721
722 **Figure 12.** Sketch showing the surface manifestations and the general movement of fluids
723 and heat at Le Biancane. Fluids upflow along cracks, faults or fractures with very steep dips
724 and preferential NW-SE and NE-SW orientation (the base of the sketch is from Hurvitz et al.,
725 2012, modified).
726
727 The heat associated to the fluid movement in volcanic-hydrothermal environments is mainly
728 transferred by conduction in the shallower part of the soil (Chiodini et al., 2005). Assuming a
729 soil thermal conductivity of the order of 1 W m^{-1} K^{-1} (Chiodini et al., 2005) and a heat flux of
730 the order of 300 W m^{-2}, we expect an average geothermal gradient of the order of 300 K m^{-1}
731 in the thin conductive region between the surface and the top of the steam condensation layer.
732 This process warms up the near-surface layer generating thermal anomalies that can be
733 mapped from the ground and from the space by Thermal InfraRed (TIR)-based observations

734 (Hochstein and Bromley, 2005; Harris, 2013). The Land Surface Temperature (LST) map
735 (Fig. 1d) and the thermal images taken from ground (Fig.s B.1 and B.2, in Appendix B)
736 highlight a significant thermal anomaly centred at Le Biancane and elongated toward the
737 north in the adjacent thermal area of Sasso Pisano village. The thermal anomaly seen from
738 space appears significantly colder than that observed from ground but this is because each
739 pixel of the image from the space is of the order of 100x100 m^2, while for images from the
740 ground the pixel is of the order of 10x10 cm^2.
741

742 **6. Conclusions**

743 Results have been presented for a multidisciplinary study in the natural degassing area of Le
744 Biancane, southern portion of the Larderello-Travale geothermal field (LTGF). LTGF is a
745 typical vapour dominated geothermal field, classified as convective dominated plutonic type
746 play (Moeck, 2014). It has been exploited for power production since 1913.
747 Compositional data of local high-T fumaroles, sampled and analyzed over the period of the
748 investigation (May-June 2021) and previously (in 2005-2006), confirmed that H_2O is the
749 main component (98-99 % mol), followed by CO_2 (0.5-1 % mol), and minor amounts of
750 H_2S, CH_4, N_2, H_2, He, Ar, CO and COS. The gases of the natural manifestations are similar in
751 chemical composition to those discharged by local geothermal production wells, but indicate
752 some mixing with air and air saturated water (ASW), at least for some samples.
753 Available data on stable isotope compositions of steam condensates (in particular those
754 referred to hydrogen) indicate that some fumaroles (e.g., B6 and B7, located in the SW sector
755 of Le Biancane) have compositions consistent with the isotope composition of the fluids
756 feeding geothermal wells affected by re-injection of spent steam, while others (e.g., B8,
757 located in the central part of Le Biancane) have similarity with the composition of geothermal

758 wells before re-injection and therefore with the primary steam and local springs. This is a
759 very interesting issue to be detailed and more data are needed for fumaroles and geothermal
760 wells condensates.
761 Gas geobarometers indicate P_{H2O} of 15.8 bar to 31.9 bar, and P_{CO2} of a few tenths of bar
762 (from 0.15 bar to 0.42 bar) in the shallow reservoir, both the intervals in agreement with
763 those estimated for local geothermal production wells.
764 A total output of 11.5±0.77 t day^{-1} CO_2 was estimated from an area of about 60,000 m^2 by
765 using geostatistical methods. The isotopic composition of $\delta^{13}C_{(CO2)}$ suggests that the
766 sedimentary formation of the Tuscan Nappe, outcropping in the Le Biancane area, is the main
767 source of CO_2, with minor contribution of magmatic and biological CO_2. The locations with
768 the most notable CO_2 degassing (CO_2 flux > 501 g m^{-2} day^{-1}) lie in some central spots of the
769 investigated area, near the fumarole areas, where highest soil temperature (> 50 °C) were
770 recorded. Because the "anomalous" zones coincide with local well-connected cracks (faults
771 and fractures), preferentially NW-SE and NE-SW trending, we believe that these cracks
772 provide preferential but temporary pathways for fluids and heat to migrate to the surface.
773 Following the approach of Chiodini et al. (2001, 2005) we estimated the thermal energy loss
774 associated with the natural degassing of Le Biancane. We calculated a thermal energy
775 ranging from 20.4 MW to 30.6 MW taking account of the main thermal contribution of the
776 vapour when it moves from reservoir conditions to the surface and the minor thermal
777 contribution of the CO_2 travelling with the rising vapour. These values are comparable with
778 the nominal capacities of the individual geothermal plants currently operating in the
779 Larderello field (most of them with nominal power of 20 MW, Razzano and Cei, 2015). This
780 energy heats conductively the near-surface layer, producing a spatial distribution of the
781 surface temperatures that are correlated with the soil CO_2 flux in the hottest central sector of
782 Le Biancane.

Future works should be aimed at better quantifying gas emissions and heat discharge and better understanding their spatial correlations, perhaps most importantly using a finer spatial resolution of the measurements' grid. Moreover, more compositional and isotope data of production wells and natural manifestations might help to clarify the complex relations between rising fluids, infiltrating meteoric waters and re-injected spent steam.

Data Availability Statement

The dataset of soil CO_2 flux and soil brightness temperature at Le Biancane can be accessed at https://zenodo.org/record/7152367

The dataset of structural measurements at Le Biancane can be accessed at https://doi.org/10.5281/zenodo.7156320

Appendix A: Fracture Network Topological Analysis

The fracture network is represented as a two-dimensional array of lines that intersects each other (Fig. A.1).

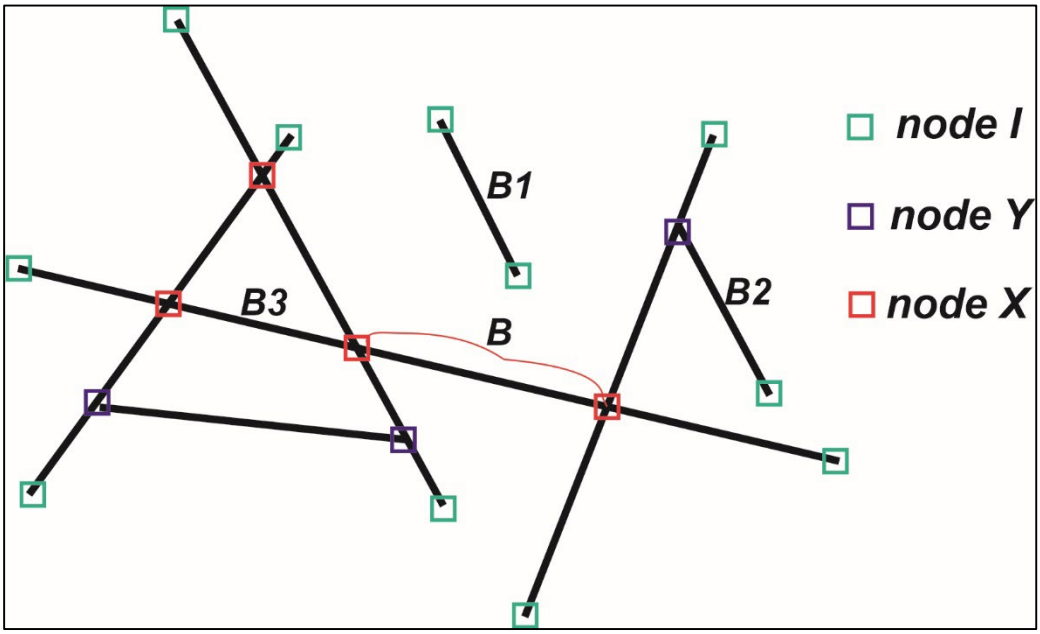

Figure A.1. Schematic model of a fracture network (modified after Sanderson and Nixon, 2015) where the fractures (lines) are divided by their intersections in branches (segments). The nodes differentiate for the number of branches that they connect.

The intersections between the fractures (in general lines) form segments that are termed branches. Each branch (B in Figure A.1) is bounded by two nodes. The nodes can be of three types: i) nodes I with only one termination (green box in Fig. A.1), ii) nodes Y with three terminations (blue box in Fig. A.1), and iii) nodes X with four terminations (red box in Fig. A.1). According to Sanderson and Nixon (2015; 2018), there is a direct geometric relationship between the number and the type of nodes and the number of lines (N_L) and branches (N_B):

$$N_L=(N_I+N_X)/2 \quad (1a)$$

$$N_B=(N_I+3N_Y+4N_X)/2 \quad (1b)$$

where N_I, N_X and N_Y are the number of nodes I, X and Y, respectively.

Being $(N_I+N_Y+N_X)$ the total number of branches, the proportion of each type of nodes is:

$$P_I=N_I/(N_I+N_Y+N_X) \quad (2a)$$

$$P_Y=N_Y/(N_I+N_Y+N_X) \quad (2b)$$

$$P_X=N_X/(N_I+N_Y+N_X) \quad (2c)$$

$$P_I + P_Y + P_X = 1 \quad (2d)$$

Each branch ends at a node (Figure A.1) and is apparent that an I-node produces one end, a Y-node produces 3 and an X-node produces 4, totalling $(N_I + 3N_Y + 4N_X)$ ends. The proportion of isolated to connected ends is $N_I/(3N_Y + 4N_X)$. Consequently, the probability of the end of any branch being an isolated (P_I) or connected (P_C) node is given by:

$$P_I = N_I/(N_I + 3N_Y + 4N_X) \quad (3a)$$

$$P_C = (3N_Y + 4N_X)/(N_I + 3N_Y + 4N_X) \quad (3b)$$

If there is a random assignment of nodes to branches the probability of each branch type is:

$$PII' = P_I^2 \quad (4a)$$

$$PIC' = P_I*P_C \quad (4b)$$

$$PCC' = P_C^2 \quad (4c)$$

$$PII' + PIC' + PCC' = 100 \quad (4d)$$

Each branch is connected to the other branches by nodes, a branch with two nodes I is not connected (e.g., B1 in Fig. A.1), a branch with a node I and a node X or Y is partially

connected (B2 in Fig. A.1) and a branch with node Y and/or X is fully connected (B3 in Fig. A.1).

Using equations (3) and (4) it is possible to compute the proportion of branches defined by nodes I and those defined by nodes Y or X. As shown in Sanderson and Nixon (2015) the probability of having non connected branches (PII'), partially connected branches (PIC') and fully connected branches (PCC') is easily derived.

Using these topological observations (Sanderson and Nixon, 2015; 2018), the number of intersections per line (C_L) and per branch (C_B) are derived as follows:

$$C_L=2(N_X+N_Y)/N_L \quad (5a)$$

$$C_B=(3N_Y+4N_X)/N_B \quad (5b)$$

C_L and C_B are a proxy of the degree of connectivity of the fracture network. When $C_L>3.57$ and $C_B>1.56$, the fracture network is very well connected. (e.g., Balberg et al.,1984; Sanderson and Nixon, 2018). As suggested in Sanderson and Nixon (2018) C_B is a better proxy for the fracture network connection than C_L.

Appendix B: Thermal infrared ground measurements

A series of thermal infrared images has been taken during the presented field activities. As described in the main text, the site shows a wide range of variability that can be qualitatively and quantitatively analysed by using infrared images. For example in Fig. B.1, a couple of snapshots are reported.

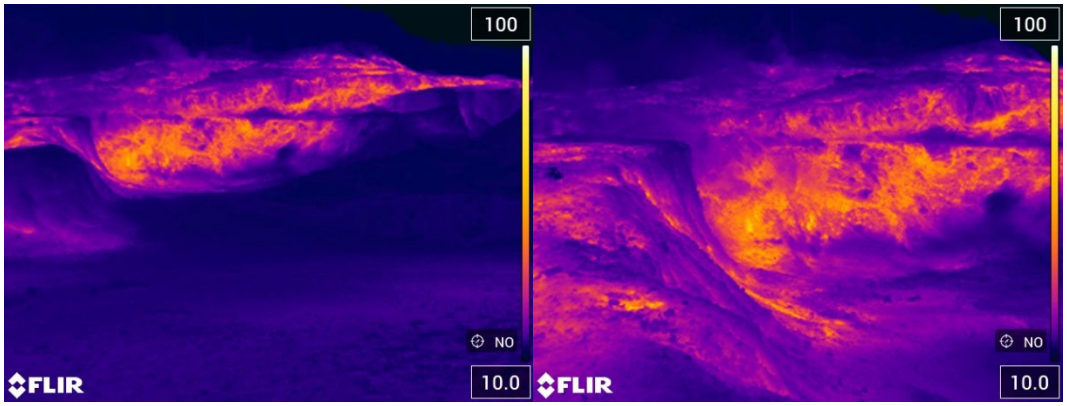

Figure B.1. The main anomalous area of Le Biancane seen from 2 different points of view. The FLIR camera E76 has been used to capture these thermal infrared images in the window 7-14 μm. The linear colorbar represents the brightness temperature in the range 10-100 °C.

The camera has a resolution of 320x240 pixels, with a field of view of 42x32 degrees. The 146 measures have been taken by positioning the camera at a height of about 1 m high, looking vertically towards the ground. Each measurement represents the soil brightness temperature averaged on the central rectangle 160x120 pixels wide (Fig. B.2). This averaging area is about 40x30 cm^2.

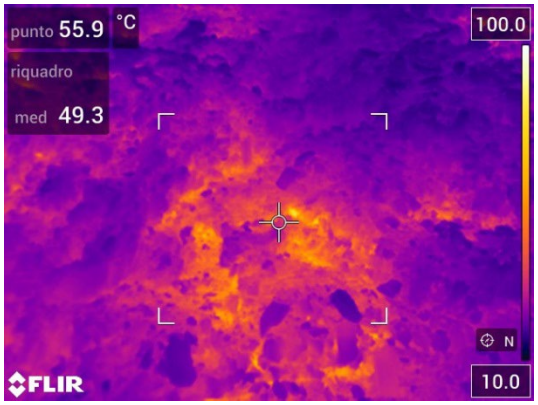

Figure B.2. Example of the field of view used to retrieve brightness temperature measurements. The linear colorbar represents the brightness temperature in the range 10-100 °C. On the top left is reported the value of the central point ("punto"), while below can be found the value averaged over the central rectangle ("med").

REFERENCES

Adler, P.M., Thovert, J.F., 1999. Fractures and Fracture Networks, vol. 15. Kluwer Academic Publishers, Dordrecht.

Arias, A., Dini, I., Casini, M., Fiordelisi, A., Perticone, I., Dell'Aiuto, P., 2010. Geoscientific Feature Update of the Larderello-Travale Geothermal System (Italy) for a Regional Numerical Modeling. Proceedings World Geothermal Congress 2010. Bali, Indonesia.

Baba, A., Şaroğlu, F., Akkuş, I., Özel, N., Yeşilnacar, M.İ., Nalbantçılar, M.T., Demir, M.M., Gökçen, G., Arslan, Ş., Dursun, N., Uzelli, T., Yazdani, H., 2019. Geological and hydrogeochemical properties of geothermal systems in the southeastern region of Turkey. Geothermics 78, 255-271. https://doi.org/10.1016/j.geothermics.2018.12.010.

Baba, A., Sözbilir, H., Sayık, T., Arslan, S., Uzelli, T., Tonkul, S., Demir, M.M., 2022. Hydrogeology and hydrogeochemistry of the geothermal systems and its direct use application: Balçova-Narlıdere geothermal system, İzmir, Turkey. Geothermics, 104, 102461. https://doi.org/10.1016/j.geothermics.2022.102461.

Barin, I., and Knacke, O., 1973. Thermochemical Properties of Inorganic Substances, pp. 921, Springer-Verlag, New York.

Barsi, J.A., Barker, J.L., Schott J.R., 2003. An Atmospheric Correction Parameter Calculator for a Single Thermal Band Earth-Sensing Instrument. IGARSS03, 21-25 July 2003, Centre de Congrès Pierre Baudis, Toulouse, France.

Barton, C.C., 1995. Fractal Analysis of Scaling and Spatial Clustering of Fractures. In: Barton, C.C., La Pointe, P.R. (eds) Fractals in the Earth Sciences. Springer, Boston, MA. https://doi.org/10.1007/978-1-4899-1397-5_8.

Batini, F., Bertini, G., Gianelli, G., Pandeli, E., Puxeddu, M., 1983. Deep structure of the Larderello field: contribution from recent geophysical and geological data. Soc. Geol. Ital. Mem. 25, 219-235.

Batini, F., Burgassi, P.D., Cameli, G.M., Nicholic, R., Squarci, P., 1978. Contribution to the study of the deep lithospheric profiles: "Deep" reflecting horizons in Larderello-Travale geothermal field. Società Geologica Italiana. Perugia, 2-4 Ottobre 1978.

898 Batini, F., Bertini, G., Gianelli, G., Pandeli, E., Puxeddu, M., Villa, I.M., 1985. Deep
899 structure, age and evolution of the Larderello-Travale geothermal field. Geotherm. Res.
900 Coun. Trans. 9, 253-259.

901 Bertrami, R., Cioni, R., Corazza, E., D'amore, F., Marini, L., 1985. Carbon monoxide in
902 geothermal gases. Reservoir temperature calculation at Larderello (Italy). Geotherm. Resour.
903 Council Int. Symp. on Geothermal Energy, August 1985, Kona, Hawaii, Trans. 9/I, 299-302.

904 Bertani, R., Bertini, G., Cappetti, G., Fiordelisi, A., Marocco, B.M., 2005. An Update of the
905 Larderello-Travale/Radicondoli Deep Geothermal System. Proceedings World Geothermal
906 Congress, Antalya, Turkey, 24-29 April 2005.

907 Bertani, R., 2016. Geothermal power generation in the world 2010-2014 update report.
908 Geothermics 60, 31-43.

909 Bertini, G., Casini, M., Ciulli, B., Ciuffi, S., Fiordelisi, A., 2005. Data revision and upgrading
910 of the structural model of the Travale geothermal field (Italy). In: Proceedings of the 2005,
911 World Geothermal Congress, Antalya, Turkey, paper 2612, pp. 8.

912 Bertini, G., Casini, M., Gianelli, G., Pandeli, E., 2006. Geological structure of a long-living
913 geothermal system, Larderello, Italy. Terra Nova 18, 163-169.

914 Bolognesi, L., 2011. The oxygen isotope exchange between carbon dioxide and water in the
915 Larderello geothermal field (Italy) during fluid reinjection. Geothermics 40 (3), 181-189.
916 https://doi.org/10.1016/j.geothermics.2011.06.002.

917 Brogi, A., Lazzarotto, A., Liotta, D., Ranalli, G., 2003. Extensional shear zones as imaged by
918 reflection seismic lines: the Larderello geothermal field (central Italy). Tectonophysics 363,
919 27 - 139. doi:10.1016/S0040-1951(02)00668-6.

920 Bromley, C.J., Hochstein, M.P., 2000. Heat transfer of the Karapiti fumarole field (1946-
921 2000). In: Proceedings of the 22nd NZ Geothermal Workshop, University of Auckland, pp.
922 87-92.

923 Cabassi, J., Venturi, S., Di Bennardo, F., Nisi, B., Tassi, F., Magi, F, Ricci, A., Picchi, G.,
924 Vaselli, O., 2021. Flux measurements of gaseous elemental mercury (GEM) from the
925 geothermal area of “Le Biancane” natural park (Monterotondo Marittimo, Grosseto, Italy):

926 Biogeochemical processes controlling GEM emission. J. Geoch. Expl. 228, 106824.
927 https://doi.org/10.1016/j.gexplo.2021.106824.

928 Calusi, B., Andronico, D., Pecora, E., Biale, E., Cerminara, M., 2020. PyTirCam-1.0: A
929 Python Model to Manage Thermal Infrared Camera Data. Remote Sensing.
930 https://doi.org/10.3390/rs12244056.

931 Cappetti, G., Parisi, L., Ridolfi, A., Stefani, G., 1995. Fifteen years of reinjection in the
932 Larderello-Valle Secolo area: analysis of the production data. Proceedings of the World
933 Geothermal Congress, 18-31 May 1995, Firenze, Italy, pp 1997-2000.

934 Cardellini, C., Chiodini, G., Frondini, F., 2003. Application of stochastic simulation to CO_2
935 flux from soil: Mapping and quantification of gas release. J. Geophys. Res. 108(B9), 2425.
936 doi:10.1029/2002JB002165.

937 Carella, M., Fulignati, P., Musumeci, G., Sbrana, A., 2000. Metamorphic consequences of
938 Neogene thermal anomaly in the northern Apennines (Radicondoli-Travale area, Larderello
939 geothermal field Italy). Geodinamica Acta 13, 6, 345-366. doi:10.1016/S0985-
940 3111(00)01051-2.

941 Casini, M., Ciuffi, S., Fiordelisi, A., Mazzotti, A., Stucchi, E., 2010. Results of a 3D seismic
942 survey at the Travale (Italy) test site. Geothermics 39, 1, 4-12.
943 doi:10.1016/j.geothermics.2009.11.003

944 Cavaretta, G., Gianelli, G., Puxeddu, M., 1983. Hydrothermal and contact metamorphism in
945 the Larderello geothermal field (Italy): a new contribution from San Pompeo deep well. 4th
946 International Symposium on Water Rock Interaction, Miassa, Japan, pp. 82-86.

947 Ceccarelli, A., Celati, R., Grassi, S., Minissale, A., Ridolfi, A., 1987. The southern boundary
948 of Larderello Geothermal field. Geothermics 16, 505-515.

949 Cerminara, M., Fasano, A., 2012. Modeling the dynamics of a geothermal reservoir fed by
950 gravity driven flow through overstanding saturated rocks. J. Volcanol. Geotherm. Res. 233-
951 234, 37-54.

952 Chiodini, G., Cioni, R., 1989. Gas geobarometry for hydrothermal systems and its application
953 to some Italian geothermal areas. Appl. Geochem. 4, 465-472.

954 Chiodini, G., Cioni, R., Raco, B., Scandiffio, G., 1991. Carbonyl sulphide (COS) in
955 geothermal fluids: An example from the Larderello Field (Italy). Geothermics 20 (5/6), 319-
956 327.

957 Chiodini, G., Cioni, R., Guidi, M., Marini, L., Raco, B., Taddeucci, G., 1992. Gas
958 geobarometry in boiling hydrothermal systems: a possible tool to evaluate the hazard of
959 hydrothermal explosions. Acta Vulcanologica Marinelli Vol. 2, 99-107.

960 Chiodini, G., Marini, L., 1998. Hydrothermal gas equilibria: The H_2O-H_2-CO_2-CO-CH_4
961 system. Geochim. Cosmochim. Acta 62, 2673-2687.

962 Chiodini, G., Cioni, R., Guidi, M., Raco, B.,Marini, L., 1998. Soil CO_2 flux measurements in
963 volcanic and geothermal areas. Appl. Geochem. 13, 543-552.

964 Chiodini, G., Frondini, F., Cardellini, C., Granieri, D., Marini, L., Ventura, G., 2001. CO_2
965 degassing and energy release at Solfatara volcano. J. Geophys. Res. 106, 16213-16221.

966 Chiodini, G., Granieri, D., Avino, R., Caliro, S., Costa, A., Werner, C., 2005. Carbon dioxide
967 diffuse degassing and estimation of heat release from volcanic and hydrothermal systems. J.
968 Geophys. Res. 110, B08204. doi:10.1029/2004JB003542.

969 Cioni, R., Corazza, E., Magro, G., Guidi, M, Marini, L., 1988. Reactive and inert gases in
970 low temperature fumaroles (Aeolian Islands, Italy). Rend. Soc. It. Min. Petr. 43, 1003-1011.

971 Cox, S.F., 2010. The application of failure mode diagrams for exploring the roles of fluid
972 pressure and stress states in controlling styles of fracture-controlled permeability
973 enhancement in faults and shear zones. Geofluids 10, 217-233. doi: 10.1111/j.1468-
974 8123.2010.00281.x.

975 Craig, H., 1961. Isotopic variations in meteoric waters. Science 133, 1702-1703.
976
977 D'Amore, F., Fancelli, R., Saracco, L., and Truesdell, A., 1987. Gas geothermometry based
978 on CO content: Application in Italian geothermal fields. Proc. 12th Work. Geothermal
979 Reservoir Eng. Stanford University, 48-53.
980
981 David, M., 1977. Geostatistical Ore Reserve Estimation. Elsevier Sci., 364 pp., New York.

982 Gat, J.R., Carmi, I., 1970. Evolution of the isotopic composition of atmospheric waters in the
983 Mediterranean area. Journal of Geophysical Research 75, 3039- 3048.

984 Gherardi, F., Panichi, C., Gonfiantini, R., Magro, G., Scandiffio, G., 2005. Isotope
985 systematics of C-bearing gas compounds in the geothermal fluids of Larderello, Italy.
986 Geothermics 34, 442-470.

987 Gianelli, G., Manzella, A., Puxeddu, M., 1997. Crustal models of the geothermal areas of
988 southern Tuscany (Italy). Tectonophysics 281, 221-239.

989 Gianelli, G., Ruggieri, G., 2002. Evidence of contact metamorphic aureole with high-
990 temperature metasomatism in the deepest part of the active geothermal of Larderello, Italy.
991 Geothermics 31, 443-474.

992 Giggenbach, W.F., 1975. A simple method for the collection and analysis of volcanic gas
993 samples. Bull. Volcanol. 39, 132- 145.

994 Giggenbach, W.F., 1980. Geothermal gas equilibria. Geochim. Cosmochim. Acta 44, 2021-
995 2032.

996 Giggenbach, W.F., 1992. Isotopic composition of geothermal water and steam discharges. In:
997 D'Amore, F. (Ed.), Application of Geochemistry in Geothermal Reservoir Development.
998 United Nations Institute for Training and Research,New York, NY, USA, pp. 253-273.

999 Giggenbach, W.F., 1996. Chemical composition of volcanic gases. In: Scarpa R and Tilling
1000 RI (eds.) Monitoring and Mitigation of Volcano Hazards, pp. 221-256. Berlin: Springer-
1001 Verlag.

1002 Granieri D., de' Michieli Vitturi M., Bisson M., 2018. Peaklocator 1.0, a Web tool to
1003 compare extreme value areas among maps. Annals of Geophysics 61 (5). doi: 10.4401/ag-
1004 7813.

1005 Gudmundsson, A., Fjeldskaar, I., Brenner, S.L., 2002. Propagation path-ways and fluid
1006 transport of hydrofracture in jointed and layered rocks in geothermal fields. J. Volcanol.
1007 Geotherm. Res. 116, 257-278. doi:10.1016/S0377-0273(02)00225-1.

1008 Hardebol, N. J., Maier, C., Nick, H., Geiger, S., Bertotti, G., Boro H., 2015. Multiscale
1009 fracture network characterization and impact on flow: A case study on the Latemar carbonate
1010 platform. J. Geophys. Res. Solid Earth 120. doi:10.1002/2015JB011879.

1011 Harris, A., 2013. Thermal remote sensing of active volcanoes: a user's manual. Cambridge
1012 University press.

1013 Hochstein, M.P., Bromley, C.J., 2005. Measurement of heat flux from steaming ground,
1014 Geothermics 34, 133-160.

1015 Hochstein, M.P., Browne, P.R.L., 2000. Surface manifestations of geothermal systems with
1016 volcanic heat sources. In: Sigurdsson, H. (Ed.), Encyclopaedia of Volcanoes. Academic
1017 Press, pp. 835-855.

1018 Hooker, P.J., Bertrami, R., Lombardi, S., O'Nions, R.K., Oxburgh, E.R., 1985. Helium-3
1019 anomalies and crust-mantle interaction in Italy, Geochim. Cosmochim. Acta 49, 2505-2513.

1020 Hurwitz, S., Robert N. Harris, R.N., Werner, C.A., Murphy, F., 2012. Heat flow in vapour
1021 dominated areas of the Yellowstone Plateau Volcanic Field: Implications for the thermal
1022 budget of the Yellowstone Caldera. J. Geophys. Res. 117 (B10207).
1023 doi:10.1029/2012JB009463.

1024 Jaccard, P., 1901. Étude comparative de la distribution florale dans une portion des Alpes et
1025 des Jura. Bulletin de la Société Vaudoise des Sciences Naturelles 37, 547-579.

1026 Keenan, J.H., Keyes, F.G., Hill, P.G., Moore, J.G., 1969. Steam Tables: Thermodynamic
1027 Properties of Water Including Vapor, Liquid, and Solid Phases, 162 pp., John Wiley,
1028 Hoboken, N. J.

1029 Lelli, M., 2021. GC-ICP-MS method as a new application for geothermal/volcanic gas
1030 characterization. 1st IAVCEI-CCVG Virtual Workshop, 24-26 May, 2021. Poster.

1031 Lemmon, E.W., Bell, H.B., Huber, M. L, McLinden, M.O., "Thermophysical Properties of
1032 Fluid Systems" in NIST Chemistry WebBook, NIST Standard Reference Database Number
1033 69, Eds. P.J. Linstrom and W.G. Mallard, National Institute of Standards and Technology,
1034 Gaithersburg MD, 20899, https://doi.org/10.18434/T4D303, (retrieved June 28, 2022).

1035 Liotta, D., Brogi, A., 2020. Pliocene-Quaternary fault kinematics in the Larderello
1036 geothermal area (Italy): Insights for the interpretation of the present stress field. Geothermics
1037 83 (2020) 101714.

1038 Magro, G., Ruggieri, G., Gianelli, G., Bellani, S., Scandiffio, G., 2003. Helium isotopes in
1039 paleofluids and present day fluids of the Larderello geothermal field: constraints on the heat
1040 source. J. Geophys. Res. 108, ECV 3-1-12.

1041 McNamara, D. D., Milicich, S. D., Massiot, C., Villamor, P., McLean, K., Sépulveda, F.,
1042 Ries, W. F., 2019. Tectonic controls on Taupo Volcanic Zone geothermal expression:
1043 Insights from Te Mihi, Wairakei Geothermal Field. Tectonics 38, 3011-3033.
1044 https://doi.org/10.1029/2018TC005296.

1045 Menichini, M., 2006. Degassamento diffuso in Italia: contributo alla valutazione del rischio
1046 gas nell'area geotermica di Larderello. Thesis in Geological Science, University of Pisa.

1047 Mineo, S., Pappalardo, G., 2021. Rock Emissivity Measurement for Infrared Thermography
1048 Engineering Geological Applications. Appl. Sci. 11, 3773.
1049 https://doi.org/10.3390/app11093773.

1050 Moeck, I.S., 2014. Catalog of geothermal play types based on geologic controls. Renewable
1051 and Sustainable Energy Reviews 37, 867-882. http://dx.doi.org/10.1016/j.rser.2014.05.032.

1052 Musumeci, G., Bocini, L., Corsi, R., 2002. Alpine tectonothermal evolution of the Tuscan
1053 Metamorphic Complex in the Larderello geothermal field (northern Apennines, Italy).
1054 Journal of The Geological Society 159, 443-456. doi:10.1144/0016-764901-084.

1055 Oliver, N.H.S., 1996. Review and classification of structural controls on fluid flow during
1056 regional metamorphism. J. Metamorphic Geol. 1996, 14, 477-492.

1057 Panichi, C., Celati, R., Noto, P., Squarci, P., Taffi, L., Tongiorgi, E., 1974. Oxygen and
1058 hydrogen isotope studies of the Larderello, Italy, geothermal system. Proceedings of the
1059 Symposium on Isotope Techniques in Groundwater Hydrology (Vienna) - IAEA, 2, 3-28.

1060 Panichi, C., Scandiffio, G., Baccarin, F., 1995. Variation of geochemical parameters induced
1061 by reinjection in the Larderello area. Proceedings of the World Geothermal Congress 1995,
1062 Florence, Italy, 1845-1949.

1063 Piccinini, D., Saccorotti, G., 2018. Observation and analyses of shear wave splitting at the
1064 Larderello-Travale geothermal field, Italy. J. Volcanol. Geotherm. Res. 363, 1-9.
1065 https://doi.org/10.1016/j.jvolgeores.2018.08.004.

1066 Razzano, F., Cei, M., 2015. Geothermal power generation in Italy 2010-2014 update report.
1067 Proceedings of the World Geothermal Congress 2015, Melbourne, Australia, 19-25 April
1068 2015.

1069 Ruggieri, G., Chatelineau, M., Boiron, M.C., Marignac, C., 1999. Boiling and fluid mixing in
1070 the chlorite zone of the Larderello geothermal system. Chem. Geology 154, 237-256.

1071 Sanderson, D.J., Nixon, C.W., 2015. The use of topology in fracture network
1072 characterization. Journal of Structural Geology 72, 55-66.

1073 Sanderson, D.J., Nixon, C.W., 2018. Topology, connectivity and percolation in fracture
1074 networks. Journal of Structural Geology 115, 167-177.

1075 Siler, D.L., Faulds, J., Mayhew, B., & Mcnamara, D.D., 2016. Analysis of the favorability for
1076 geothermal fluid flow in 3D: Astor Pass geothermal prospect, Great Basin, northwestern
1077 Nevada, USA. Geothermics 60, 1-12.

1078 Silvestri, M., Marotta, E., Buongiorno, M.F., Avvisati, G., Belviso, P., Bellucci Sessa, E.,
1079 Caputo, T., Longo, V., De Leo, V., Teggi, S., 2020. Monitoring of Surface Temperature on
1080 Parco delle Biancane (Italian Geothermal Area) Using Optical Satellite Data, UAV and Field
1081 Campaigns. Remote Sens. 12. doi:10.3390/rA12122018.

1082 Sinclair, A.J., 1974. Selection of thresholds in geochemical data using probability graphs. J.
1083 Geochem. Expl. 3, 129-149.

1084 Tarchini, L., Carapezza, M.L., Granieri, D., Frepoli, A., Pagliuca, N.M., Ranaldi, M., 2022.
1085 Twenty Years Monitoring of Soil CO_2 Flux and Seismicity at Cava dei Selci Gas Discharge
1086 (Colli Albani Volcano, Italy). Earth and Space Science 2022, 9, e2021EA001936.
1087 https://doi.org/10.1029/2021EA001936.

1088 Taussi, M., Brogi, A., Liotta, D., Nisi, B., Perrini, M., Vaselli, O., Zambrano, M., Zucchi, M.,
1089 2022. CO_2 and heat energy transport by enhanced fracture permeability in the Monterotondo

1090 Marittimo-Sasso Pisano transfer fault system (Larderello Geothermal Field, Italy).
1091 Geothermics 105, 102531. doi: https://doi.org/10.1016/j.geothermics.2022.102531.

1092 Torgersen, T., 1980. Controls on pore-fluid concentration of ^{4}He and ^{222}Rn and the
1093 calculation of $^{4}He/^{222}Rn$ ages. J. Geochem. Explor. 13, 57-75.

1094 Truesdell, A.H., White, D.E., 1973. Production of superheated steam from vapor-dominated
1095 geothermal reservoirs. Geothermics 2, 154-173.

1096 Uzelli, T., Mungan, G.G., Baba, A., Sözbilir, H, Dirik, K., 2017. The conceptual model of the
1097 Gülbahçe geothermal system, Western Anatolia, Turkey: Based on structural and
1098 hydrogeochemical data. Geothermics, 68, 67-85.
1099 https://doi.org/10.1016/j.geothermics.2017.03.003.

1100 Uzelli, T., Şener, M.F., Dölek, İ., Baba, A., Sözbilir, H., Dirik, R.K., 2021. Structural
1101 controls and hydrogeochemical properties of geothermal fields in the Varto Region, East
1102 Anatolia. Turkish Journal of Earth Sciences. doi: 10.3906/yer-2106-13.

1103 Venturi, S., Tassi, F., Magi, F., Cabassi, J., Ricci, A., Capecchiacci, F., Caponi, C., Nisi, B.,
1104 Vaselli, O., 2019. Carbon isotopic signature of interstitial soil gases reveals the potential role
1105 of ecosystems in mitigating geogenic greenhouse gas emissions: case studies from
1106 hydrothermal systems in Italy. Sci. Total Environ. 655, 887-898.

1107

Supplementary material

Supplementary material includes Table 1 where chemical and isotope composition of geothermal fluids are reported. Gas concentrations are expressed in μmol/mol. T(°C) for geothermal wells represent the well head temperatures (WHT). GCT is the geochemical temperature calculated on the basis of geothermometric expression of Bertrami et al. (1985). P_{H2O} and P_{CO2} estimates are based on function for pure water and on H_2S/COS ratio, respectively.

Table 1. Chemical and isotope data of geothermal fluids. The gas concentrations are expressed in μmol/mol. T(°C) for geothermal wells represent the well head temperatures (WHT). GCT is the geochemical temperature calculated on the basis of geothermometric expression of Bertrami et al. (1985). P_{H2O} and P_{CO2} estimations are based on function for pure water (equation 7) and on H_2S/COS ratio, respectively.

Code	Ref.	Date	T(°C)	X_UTM_WGS84	Y_UTM_WGS84	H_2O	CO_2	$S_{tot\ (as\ H2S)}$	N_2	O_2	Ar	CH_4	H_2	He	CO	COS	δD‰	$\delta^{18}O$‰	$\delta^{13}C$‰$_{(CO2)}$	$\delta^{18}O$‰$_{(CO2)}$	GCT	P_{H2O}	$P_{CO2\ (H2S/COS)}$	$P_{CO2\ (H2/CO)}$
Natural gas manifestations																								
B6	This study	16/06/2021	110.5	650727	4779447	994355	4842	142	190	<0.1	1.78	159	311	0.068	0.028	0.004	-36.2	-3.63	-2.78	-7.32	221	23.2	0.69	0.27
B7	This study	16/06/2021	115.3	650744	4779472	993666	5510	149	65	<0.1	0.367	204	405	0.084	0.056	0.003	-36.4	-3.83	-2.67	-7.28	238	31.9	0.56	0.42
B8	This study	16/06/2021	99.0	650913	4779731	991907	7222	203	65	<0.1	0.367	196	406	0.126	0.020	0.002	-44.3	-5.01	-2.35	-6.80	202	15.8	0.23	0.15
B1	This study	21/11/2005	99.9	650806	4779608	987750	10750	256	166	28	n.m.	442	582	0.24	0.024	n.m.	n.m.	n.m.	-3.92	-11.05	192	12.8	-	0.13
B2	This study	16/11/2005	99.3	650808	4779576	985491	11314	186	1415	274	14.3	469	549	0.37	0.099	n.m.	n.m.	n.m.	-4.19	-9.14	233	29.1	-	0.55
B3	This study	16/11/2005	100	650901	4779706	981405	16473	429	196	15	5.00	657	805	0.37	0.037	n.m.	n.m.	n.m.	-4.08	-9.83	192	12.8	-	0.14
B4	This study	16/11/2005	100	650889	4779745	983125	15042	370	178	10	2.00	566	696	0.51	0.034	n.m.	n.m.	n.m.	-4.13	-10.52	192	12.8	-	0.14
SP1	This study	20/11/2005	99.9	651738	4781116	943083	52691	1009	527	71	2.00	969	1574	1.36	0.057	n.m.	n.m.	n.m.	-4.05	-12.94	177	9.1	-	0.11
P1	This study	27/07/2006	98.8	649467	4783117	991508	6203	97	130	49	2.40	369	1642	0.148	0.016	n.m.	n.m.	n.m.	n.m.	n.m.	192	12.8	-	0.03
B6	This study	25/07/2006	129.4	650732	4779451	991687	7219	97	249	43	2.63	271	373	n.d.	0.074	n.m.	n.m.	n.m.	n.m.	n.m.	239	32.4	-	0.6
SP2	This study	26/07/2006	99.4	650982	4781584	965911	31888	614	283	n.m.	n.m.	518	771	n.d.	n.d.	n.m.	n.m.	n.m.	n.m.	n.m.	-	-	-	-
LS1	This study	25/07/2006	96.7	651809	4780969	984233	14642	195	221	22	4.75	235	413	2.36	0.016	n.m.	n.m.	n.m.	n.m.	n.m.	178	9.3	-	0.11
V1	This study	27/07/2006	97.3	651000	4780327	990918	8229	93	221	29	27.0	91	363	n.d.	0.009	n.m.	n.m.	n.m.	n.m.	n.m.	181	10.0	-	0.07
V2	This study	27/07/2006	95.2	651006	4780333	987065	11905	266	108	23	3.51	112	492	n.d.	0.013	n.m.	n.m.	n.m.	n.m.	n.m.	182	10.2	-	0.08
V3	This study	28/07/2006	99	651063	4780885	989811	9592	222	125	19	15.0	37	161	n.d.	0.020	n.m.	n.m.	n.m.	n.m.	n.m.	207	17.6	-	0.38
Mr1	Chiodini and Marini, 1998	14/11/1991	99	n.m.	n.m.	988700	10020	352	119	n.d.	n.d.	434	380	n.d.	0.011	n.m.	n.m.	n.m.	n.m.	n.m.	172	8.1	-	0.09
Mr2	Chiodini and Marini, 1998	14/11/1991	99	n.m.	n.m.	992400	6794	198	100	n.d.	n.d.	294	254	n.d.	0.010	n.m.	n.m.	n.m.	n.m.	n.m.	180	9.8	-	0.12
Mr3	Chiodini and Marini, 1998	14/11/1991	99	n.m.	n.m.	987400	11260	274	148	n.d.	n.d.	494	427	n.d.	0.019	n.m.	n.m.	n.m.	n.m.	n.m.	183	10.5	-	0.13
Geothermal wells																								
M21	Chiodini and Cioni, 1991	n.a.	248	n.a.	n.a.	990300	8020	312	n.d.	n.d.	n.d.	408	679	n.d.	0.11	0.007	n.m.	n.m.	n.m.	n.m.	246	36.7	0.68	0.49
P.141	Chiodini and Cioni, 1991	n.a.	240	n.a.	n.a.	970100	27000	921	n.d.	n.d.	n.d.	299	918	n.d.	0.22	0.039	n.m.	n.m.	n.m.	n.m.	241	33.6	1.25	0.72
SV9	Chiodini and Cioni, 1991	n.a.	229	n.a.	n.a.	801400	191000	775	n.d.	n.d.	n.d.	2540	1410	n.d.	1.81	0.099	n.m.	n.m.	n.m.	n.m.	245	36.1	3.83	3.91
P.157	Chiodini and Cioni, 1991	n.a.	203	n.a.	n.a.	830800	162000	1120	n.d.	n.d.	n.d.	728	1660	n.d.	1.29	0.102	n.m.	n.m.	n.m.	n.m.	248	38.0	2.77	2.37
P2	Chiodini and Cioni, 1991	n.a.	185	n.a.	n.a.	985400	12600	362	n.d.	n.d.	n.d.	590	721	n.d.	0.09	0.007	n.m.	n.m.	n.m.	n.m.	225	25.0	0.53	0.38
P.100	Chiodini and Cioni, 1991	n.a.	217	n.a.	n.a.	984400	14700	317	n.d.	n.d.	n.d.	12	323	n.d.	0.13	0.011	n.m.	n.m.	n.m.	n.m.	267	52.3	1.13	1.23
S3	Chiodini and Cioni, 1991	n.a.	155	n.a.	n.a.	976400	22300	330	n.d.	n.d.	n.d.	137	514	n.d.	0.05	0.005	n.m.	n.m.	n.m.	n.m.	205	16.9	0.38	0.29
Z	Chiodini and Cioni, 1991	n.a.	186	n.a.	n.a.	984300	14200	339	n.d.	n.d.	n.d.	105	444	n.d.	0.05	0.006	n.m.	n.m.	n.m.	n.m.	217	21.5	0.47	0.34
L.R.A.	Chiodini and Cioni, 1991	n.a.	191	n.a.	n.a.	961200	35400	749	n.d.	n.d.	n.d.	497	1600	n.d.	0.21	0.027	n.m.	n.m.	n.m.	n.m.	229	27.0	1	0.4
Lago8	Chiodini and Cioni, 1991	n.a.	190	n.a.	n.a.	995400	3330	396	n.d.	n.d.	n.d.	56	572	n.d.	0.14	0.005	n.m.	n.m.	n.m.	n.m.	299	85.2	0.46	0.76
LUST5	Chiodini and Cioni, 1991	n.a.	225	n.a.	n.a.	950200	44100	1390	n.d.	n.d.	n.d.	1180	2150	n.d.	0.89	0.075	n.m.	n.m.	n.m.	n.m.	265	50.6	1.75	1.27
P1	Chiodini and Cioni, 1991	n.a.	246	n.a.	n.a.	972400	24100	784	n.d.	n.d.	n.d.	538	1680	n.d.	0.46	0.028	n.m.	n.m.	n.m.	n.m.	265	50.6	1.16	0.84

n.m. - not measured
n.d. - not determined
n.a. - not available